Search for a New Charged Heavy Vector Boson Decaying to an $e\nu$ Pair in $p\bar{p}$ Collisions at $\sqrt{s} = 1.96$ TeV

Jieun Kim

Department of Physics, Major in Particle Physics

The Graduate School

June 2005

The Graduate School

Kyungpook National University

Search for a New Charged Heavy Vector Boson Decaying to an $e\nu$ Pair in $p\bar{p}$ Collisions at $\sqrt{s} = 1.96$ TeV

Jieun Kim

Department of Physics, Major in Particle Physics

The Graduate School

Supervised by Professor DongHee Kim

Approved as a qualified thesis of Jieun Kim
for the degree of Doctor of Science
by the Evaluation Committee

June 2005

Chairman　　　_____

_____

_____

_____

_____

The Graduate School Council, Kyungpook National University

TABLE OF CONTENTS

LIST OF FIGURES

iv

LIST OF TABLES

CHAPTER I

Theoretical Motivation

This thesis describes a search for a W' boson decaying into an electron and neutrino pair. A W' boson is a charged heavy vector boson that appears in the enlarged $SU(2)_L \times U(1)_Y$ gauge group of the standard model. Of the extended standard models, left-right symmetric models [1] feature a right-handed $SU(2)$ and corresponding new gauge bosons including a heavy right-handed W' denoted W_R. This analysis has been performed assuming that a right-handed neutrino decayed from the W' boson is kinematically allowed ($m_\nu \ll M_{W'}$). Here, the simplest left-right symmetric extensions of the standard model, which merely expand the gauge boson and Higgs boson sectors, will be briefly discussed.

1.1 Left-Right Symmetric Model

The left-right (LR) symmetric theories [1] predict physics beyond the standard model. The LR theories provide a renormalizable framework for

describing the origin of parity violation in weak interactions. They incorporate the $U(1)$ generator of electroweak symmetry in terms of the baryon number minus lepton $(B - L)$ [2]. For an appropriately chosen Higgs sector, they explain a smallness of the ordinary neutrino masses [3] by relating this smallness to the observed suppression of $V + A$ currents in low energy weak processes.

The LR symmetric models are based on the gauge group $SU(2)_L \times SU(2)_R \times U(1)_{B-L}$ with the quarks and leptons assigned to multiplets with quantum numbers as $Q_L : (\frac{1}{2}, 0, \frac{1}{3}), Q_R : (0, \frac{1}{2}, \frac{1}{3}), L_L : (\frac{1}{2}, 0, -1)$, and $L_R : (0, \frac{1}{2}, -1)$. Here the quantum numbers are in the order $(I_L, I_R, B - L)$. There are two free gauge couplings in this model: $g_L \equiv g$ and g_R for the $SU(2)$ groups and g' for the $U(1)_{B-L}$ group. The electric charge formular for the model is

$$(1.1) \qquad Q = I_{3L} + I_{3R} + \frac{B - L}{2}$$

In order to accomplish the LR symmetry breaking, the simplest form of the LR symmetric model requires three Higgs field multiplets, which are donoted as Δ_L, Δ_R and Φ. The Φ preserves LR symmetry and gives masses to fermions after the symmetry breaking, Δ_L and Δ_R are in the left-right symmetric multiplet. The symmetry breaking pattern is as

$$(1.2) \qquad SU(2)_L \times SU(2)_R \times U(1)_{B-L} \rightarrow SU(2)_L \times U(1)_Y \rightarrow U(1)_{EM}$$

The first stage of the symmetry breaking gives the masses to W_R and Z_R bosons which are bosons in the right-handed sector corresponding to the standard model W and Z bosons, respectively. The subsequent stage of the symmetry breaking gives the masses to the W_L and Z_L bosons which are equivalent to the standard model W and Z bosons. The observable bosons W and W' are mixtures of W_L and W_R. The general Lagrangian that describes the interactions of the W, W' to fermions is written as [4]

$$(1.3) \qquad L = -\frac{1}{\sqrt{2}} \bar{f}_i \gamma_\mu [(g_L cos\zeta V^L_{f_i f_j} P_L - g_R e^{i\omega} sin\zeta V^R_{f_i f_j} P_R) W$$

$$+ (g_L sin\zeta V^L_{f_i f_j} P_L + g_R e^{i\omega} cos\zeta V^R_{f_i f_j} P_R) W'] f_j + H.c.$$

where ζ is a left-right mixing angle and ω is a CP-violating phase that can be absorbed into V^R. $P_{R,L} = (1 \pm \gamma_5)/2$, the $g_{R(L)}$ is the right (left) gauge coupling in $SU(2)$ and $V^{R,L}_{f_i f_j}$ are either the Cabibbo-Kobayashi-Maskawa (CKM) matrix or diagonal for quarks and leptons respectively. The left-right mixing angle is assumed to be zero [5] throughout this thesis and thus W_R and W_L bosons are regarded as physical bosons which are referred to as W' and W bosons respectively. The already discovered W boson couples mostly to left-handed currents. The W' boson, which must be heavier than the W boson, couples mainly to right-handed currents. In the fermion sector, they contain the usual quarks and leptons, three light neutrino mass eigenstates $\nu_i (i = 1, 2, 3)$, and three heavy neutrino mass eigenstates $N_i (i = 1, 2, 3)$. The masses of the standard W and Z are derived primarily from

3
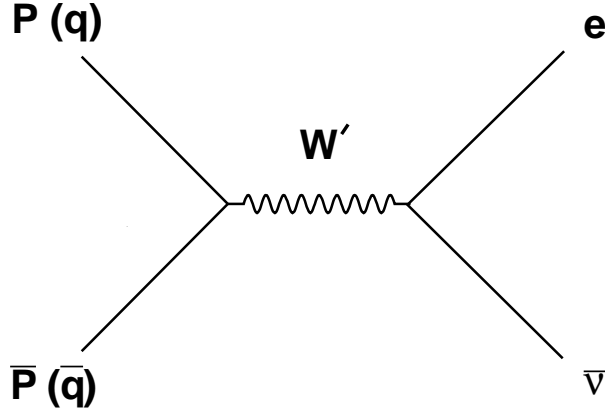
Figure 1.1: Feynman diagram for W' boson production in $p\bar{p}$ collisions at leading order.

the vacuum expectation values, κ and κ', of the two neutral members of the doublet field, Φ. The experimental result from $K_L - K_S$ mass difference, independently of the value of ζ, constrained the W' boson to be very heavy (> 1.6 TeV), assuming that the right-handed CKM matrix is the same as the left-handed CKM matrix [6]. Thus, an additional Higgs representation, with large vacuum expectation value (v_R, with $v_R \gg \kappa, \kappa'$) for its neutral member, is required that couples primarily to the W' boson. Further details on the Higgs representation describe in Ref. [7].

1.2 Production and Decay of a W' Boson

The leading order, with no gluon emission, production mechanism for a W' boson in a $p\bar{p}$ collision is quark and anti-quark annihilation as shown in Figure 1.1.

In resonance production at $p\bar{p}$ colliders [8], the two partons that enter the hard interaction do not carry the total beam momentum, but only fractions x_1 and x_2, respectively. The energy distributions of these partons are described by Parton Distributions Functions (PDF). The partons within a proton or antiproton are the valence quarks, gluons and sea quarks. The valence quarks are the bound state quarks that define the quantum numbers of the baryon and the sea quarks are a virtual quark-antiquark pair produced from the splitting of a gluon. The PDF gives the probability that a specific parton will have a fraction, x, of the proton/anti-proton momentum. Then for an interaction between two partons, the square of the scattering partons energy is $x_1 \cdot x_2 \cdot s$, where s is the square of the center-of-mass energy of the colliding particles. For the production of lepton pairs in final state having invariant mass $\sqrt{Q^2}$, the squared invariant mass of the two partons is defined as

$$(1.4) \qquad Q^2 = \hat{s} = (p_1 + p_2)^2 = x_1 x_2 s$$

where $p_1 = E_{beam}(x_1; 0, 0, x_1)$, $p_2 = E_{beam}(x_2; 0, 0, -x_2)$ and Q is momentum transfer between the particles. here, τ and y may be expressed with x_1 and x_2,

$$(1.5) \qquad \tau = x_1 x_2 = \hat{s}/s$$

$$(1.6) \qquad y = \frac{1}{2} \ln \frac{x_1}{x_2}$$

The hadronic cross section formula using the structure functions $f_1(x)$ takes the form,

$$(1.7) \qquad \sigma = \int \int \frac{d\tau}{\tau} dy x_1 f_1(x_1, Q^2) x_2 f_2(x_2, Q^2) \hat{\sigma}(\hat{s})$$

where $\hat{\sigma}$ is the matrix element cross section for the parton interaction. The cross sections can be given in the zero-width approximation, i.e. $\hat{\sigma} \propto \delta(\hat{s} - m_R^2)$, where m_R is the mass of the resonance. Introducing the scaled mass $\tau_R = m_R^2/s$, this corresponds to a delta function $\delta(\tau - \tau_R)$, which can be used to eliminate the integral over τ. Now, the delta function can be replaced by the Breit-Wigner shape. For a resonance width Γ_R,

$$(1.8) \qquad \delta(\tau - \tau_R) \rightarrow \frac{s}{\pi} \frac{m_R \Gamma_R}{(s\tau - m_R^2)^2 + m_R^2 \Gamma_R^2}$$

Here, the width is made $\hat{s}$ dependent can give improved resonance shapes. To be more precise, the Breit-Wigner is written as

$$(1.9) \qquad \delta(\tau - \tau_R) \rightarrow \frac{s}{\pi} \frac{H_R(s\tau)}{(s\tau - m_R^2)^2 + H_R^2(s\tau)}$$

The H_R factor is evaluated as a sum over all possible final-state channels. There are some interest to consider the observable resonance shape when the effects of parton distributions are included. In a hadron collider, to the first approximation, parton distributions tend to have a behaviour roughly like $f(x) \propto 1/x$ for small x. Instead, the basic parton-distribution behaviour is shifted into the factor of $1/\tau$ in the integration phase space $d\tau/\tau$. When
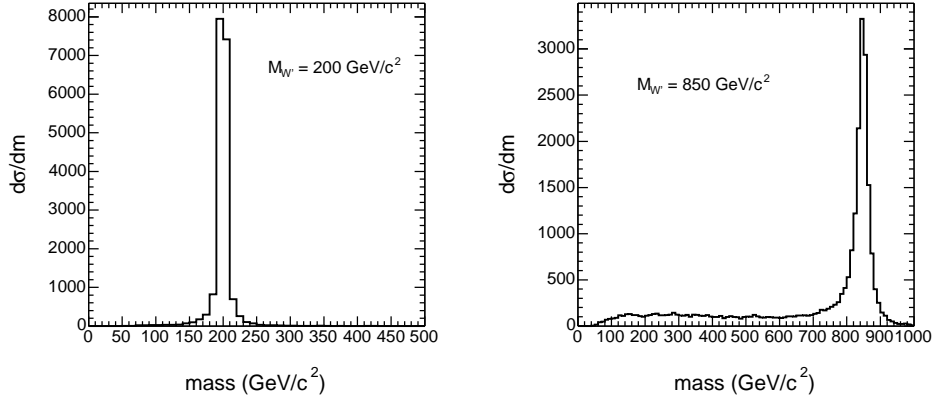
Figure 1.2: Invariant mass distributions for resonance productions of W' bosons.

convoluted with the Breit-Wigner shape, two effects appear. One is that the overall resonance is tilted: the low-mass tail is enhanced and the high-mass one suppressed. The other is that an extremely long tail develops on the low-mass side of the resonance. Shown in Figure 1.2 and 1.3 are the invariant and transverse mass distributions for W' bosons respectively. The transverse mass distributes blunter due to the smaller sizes of energy calculated in transverse directions.

Since there is a considerable discrepancy between the predictions of the Born approximation and experimental data, it is commonly accepted that the ratio between the measured cross section and the Born approximation, generally called the K-factor, can be explained by including the higher-order corrections for $\alpha_s(Q^2)$, running strong coupling constant.[1] The production

---

[1] $\alpha_s(Q^2)$ decreases with increasing Q^2 and therefore becomes small for short-distance interactions. The
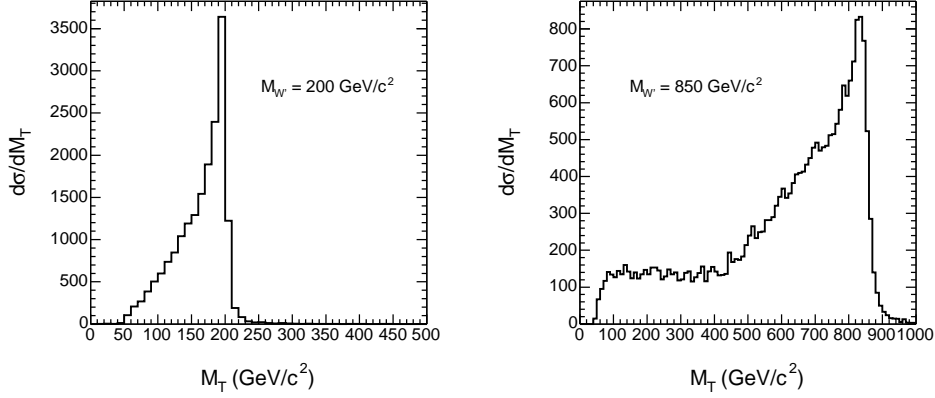
Figure 1.3: Transverse mass distributions in parton level for W' bosons.

cross section of a W' boson from this high order correction of QCD (Quantum Chromodynamics) effect will be discussed in Section 6.3.

The partial width [10] of a W' boson to a fermion pair f_i and $\bar{f}_j$ is

$$(1.10) \qquad \Gamma_{ij} = \frac{N_c G_F M_W^2 M_{W'}}{6\sqrt{2}} |V_{ij}|^2$$

where N_c is the color factor, which is three for the standard model as well as the manifest left-right symmetric model[2] and V_{ij} is the quark mixing (CKM) matrix elements.

The total width of the W' boson used in this analysis was determined assuming the standard strength couplings, and also accounted for the top

renormalized the QCD "running coupling constant" may be written [9], $\alpha_s(Q^2) = \frac{12\pi}{(33-2n_f)log(Q^2/\Lambda^2)}$, where n_f is the number of quark flavors, and Λ is the renormalization scale.

[2]The left-right symmetric model with the identical CKM matrices and the coupling constant for both left and right-handed sectors is referred to as the manifest left-right symmetric model.
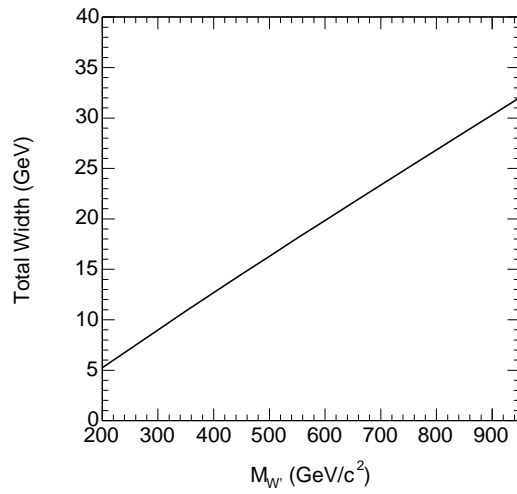
Figure 1.4: The total width for W' boson as a function of the mass.
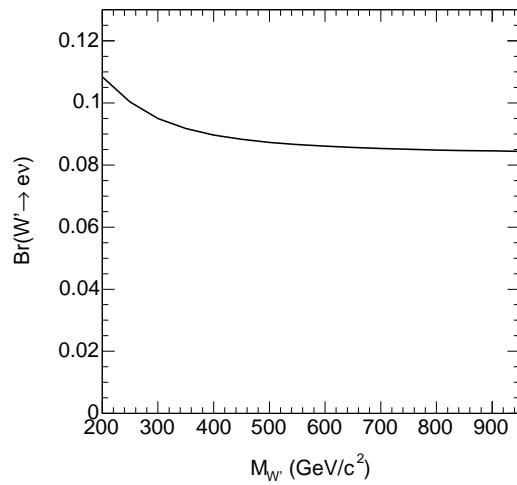
Figure 1.5: The branching fraction for $W' \rightarrow e\nu$ as a function of the mass of W' boson.

quark contribution.

(1.11) $$\Gamma(W' \to all) = \Gamma(W' \to q\bar{q}) + \Gamma(W' \to l\bar{\nu})$$

Here, it is known that the boson pair decay channel, $W' \to WZ$, is suppressed in extended gauge models and its branching fraction is independent of a W' boson mass [11]. Thus this decay channel is ignored in this analysis.

The braching fraction for $W' \to e\nu$ is calculated by

(1.12) $$Br(W' \to e\nu) = \frac{\Gamma(W' \to e\nu)}{\Gamma(W' \to all)}$$

The total width and the branching fraction for $W' \to e\nu$ as a function of the W' boson mass are shown in Figure 1.4 and 1.5, respectively.

1.3 Previous Searches

Previous searches for additional force carriers such as W' and Z' bosons have been conducted. These searches have set model dependent limits on the rate at which such a particle is produced and its mass. The most sensitive searches have been performed at the Fermilab Tevatron Collider. A Z' boson with a mass below 690 GeV/c^2 has been excluded at 95% confidence level (C.L.) [12]. Searches considering both decay models $W' \to e\nu_e$ and $\mu\nu_\mu$ have excluded a W' boson with mass below 786 GeV/c^2 at 95% C.L. [13]. These mass limits all assume that the new vector boson's couplings to leptonic final states will be given by the standard model, which predicts that the total

width of the boson increases linearly with $M_{W'}$, where $M_{W'}$ is the mass of the boson. A variety of experiments have searched for a right-handed charged-current interaction by looking for departures from the expected $V - A$ angular distribution in polarized muon decay. In this way a lower limit of 875 GeV/c^2 with 90% C.L. was obtained for the mass of the W_R, assuming a light right handed neutrino ($m_{\nu_R} < 10$ MeV/c^2). The limit weakens to > 715 GeV/c^2 if $W_L - W_R$ mixing is allowed [14].

CHAPTER II

Accelerator and Detector

The Tevatron proton-antiproton collider is the highest-energy particle collider currently operational anywhere in the world. The Tevatron accelerates and collides protons and antiprotons in a four-mile-long underground ring. Fermilab scientists use a chain of accelerators to produce and accelerate these particles before injecting them into the Tevatron ring. At Fermilab, two huge detectors called CDF (the Collider Detector at Fermilab) and D0, both consisting of many different detection subsystems, are located in the Tevatron beamline. The particle collisions take place at the centers of these collider detectors. The detectors observe the collisions, recognize the particles that come flying out and record all information for later analysis.

2.1 Accelerator

To create the world's most powerful particle beams, Fermilab uses a series of accelerators. Figure 2.1 shows the paths taken by protons and antiprotons.
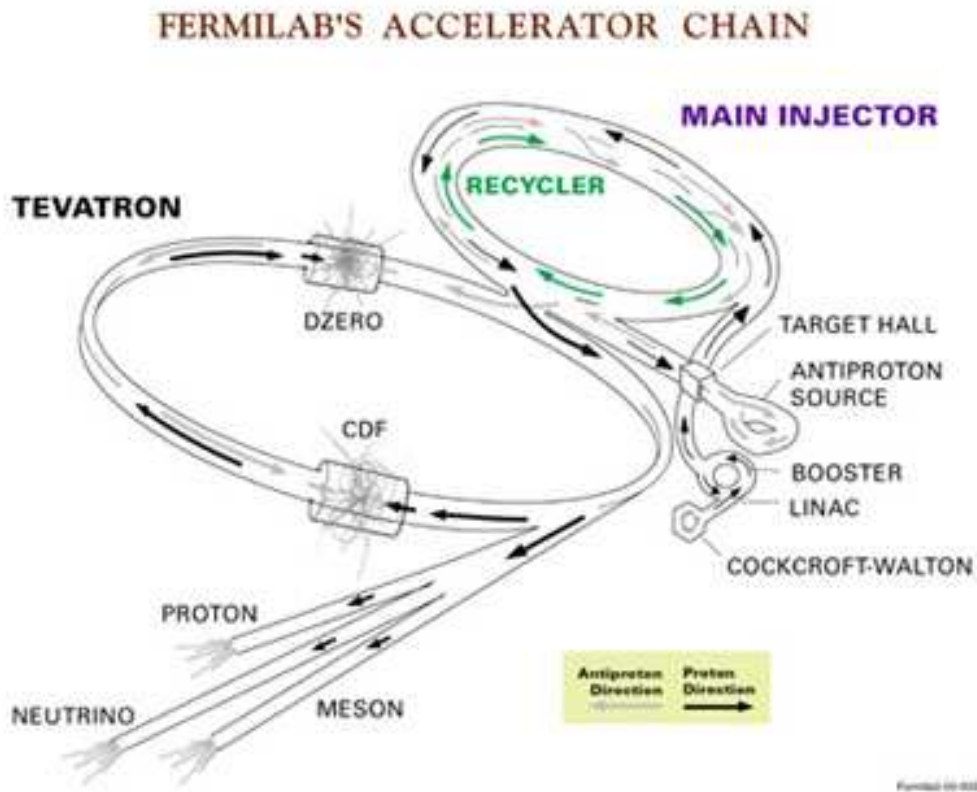
Figure 2.1: Diagram of Fermi Acclerators

The Cockcroft-Walton pre-accelerator provides the first stage of acceleration. Inside this device, hydrogen gas is ionized to create negative ions, each consisting of two electrons and one proton. The ions are accelerated by

a positive voltage and reach an energy of 750,000 electron volts (750 KeV).

Next, the negative hydrogen ions enter a linear accelerator, approximately 500 feet long. Oscillating electric fields accelerate the negative hydrogen ions to 400 million electron volts (400 MeV). Before entering the third stage, the ions pass through a carbon foil, which removes the electrons, leaving only the positively charged protons.

The third stage, the Booster, is located about 20 feet below ground. The Booster is a circular accelerator that uses magnets to bend the beam of protons in a circular path. The protons travel around the Booster about 20,000 times so that they repeatedly experience electric fields. With each revolution the protons pick up more energy, leaving the Booster with 8 billion electron volts (8 GeV).

The Main Injector, completed in 1999, accelerates particles and transfers beams. It has four functions: (1) It accelerates protons from 8 GeV to 150 GeV. (2) It produces 120 GeV protons, which are used for antiproton production. (3) It receives antiprotons from the Antiproton Source and increases their energy to 150 GeV. (4) It injects protons and antiprotons into the Tevatron.

To produce antiprotons, the Main Injector sends 120 GeV protons to the Antiproton Source, where the protons collide with a nickel target. The collisions produce a wide range of secondary particles including many an-

tiprotons. The antiprotons are collected, focused and then stored in the Accumulator ring. When a sufficient number of antiprotons has been produced, they are sent to the Main Injector for acceleration and injection into the Tevatron. Inside the Main Injector tunnel, physicists have also installed an Antiproton Recycler. It stores antiprotons that return from a trip through the Tevatron, waiting to be re-injected.

The Tevatron receives 150 GeV protons and antiprotons from the Main Injector and accelerates them to almost 1000 GeV, or one tera electron volt (1 TeV). Traveling only 200 miles per hour slower than the speed of light, the protons and antiprotons circle the Tevatron in opposite directions. The beams cross each other at the centers of the 5000-ton CDF and D0 detectors located inside the Tevatron tunnel, creating bursts of new particles.

2.2 CDF II Detector

The CDF II detector, upgraded CDF detector from Run I in 1992 - 1995 period, is an azimuthal and forward-backward symmetric apparatus designed to study $p\bar{p}$ collisions at the Tevatron. It is a general purpose solenoidal detector which combines precision charged particle tracking with fast projective calorimetry and fine grained muon detection. The detector is shown in Figure 2.2 .

Tracking systems are contained in a superconducting solenoid, 1.5m in radius and 4.8m in length, which generates a 1.4 T magnetic field parallel to

CENTRAL DRIFT CHAMBER

ELECTROMAGNETIC
CALORIMETER

EM SHOWER
MAXIMUM CHAMBER

HADRONIC CALORIMETER

MUON DRIFT CHAMBERS

STEEL SHIELDING

MUON SCINTILLATOR
COUNTER

ISL (3 LAYERS)

SVX II (3 BARRELS)

INTERACTION POINT (B0)

SOLENOID COIL

PRESHOWER DETECTOR

SHOWERMAX DETECTOR

EL – 745 FT.

UPPER NOTCH STEEL

END
PLUG
PMT
BOX

END
PLUG
PMT
BOX

Q4

EL – 706 FT.

| 0 | 1m | 2m | 3m | 4m | 5m |

| 0 | 2 | 4 | 6 | 8 | 10 | 12 | 14 | 16 ft. |

Figure 2.2: Elevation view of one half of the CDF detector.

the beam axis. Calorimetry and muon systems are all outside the solenoid.

The main features of the detector systems are summarized below. We use a coordinate system where the polar angle θ is measured from the proton directrion, the azimuthal angle ϕ is measured from the Tevatron plane, and the pseudo-rapidity is defined as $\eta = -\ln(\tan(\theta/2))$.

2.2.1 Tracking Systems

The tracking system consistes of a silicon microstrip system and of an open-cell wire drift chamber that surrounds the silicon system (see Fig-
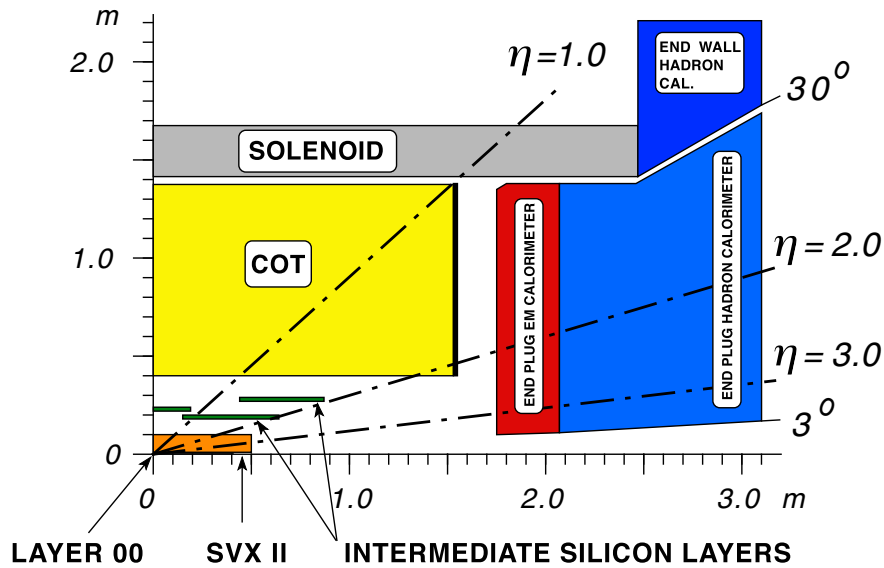
Figure 2.3: A cutaway view of one quadrant of the inner portion of the CDF II detector showing the tracking region surrounded by the solenoid and endcap calorimeters.

ure 2.3).

The silicon microstrip detector consists of seven layers (eight layers for $1.0 < |\eta| < 2.0$) in a barrel geometry that extends from a radius of r = 1.5cm from the beam line to r = 28cm.

The layer closest to the beam pipe is a radiation-hard, single sided detector called Layer 00 (L00). This enables good signal-to-noise performance even after extreme radiation doses. The remaining seven layers are radiation-hard, double sided detectors. The first five layers comprise the Silicon Vertex Detector (SVX II) system and the two outer layers comprise the Intermediate Silicon Layers (ISL) system. This entire system allows

17
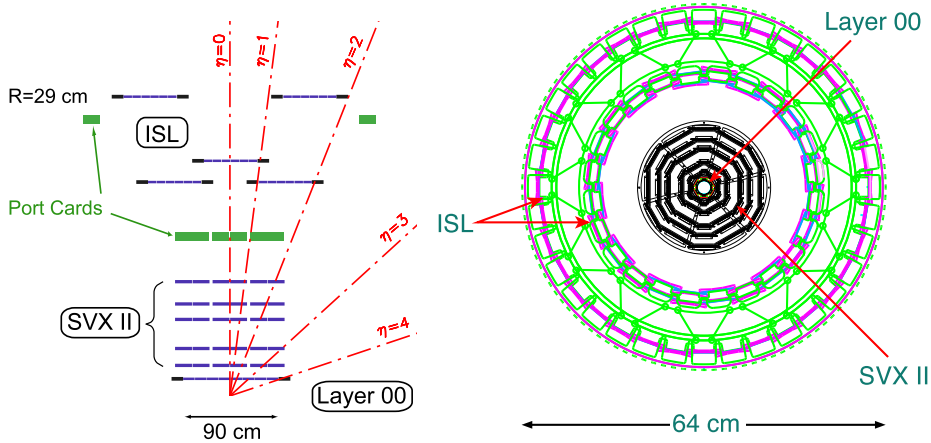
Figure 2.4: (Left) A side view of half of the CDF Run II silicon system on a scale in which the z coordinate is highly compressed. (Right) An end view of the CDF II silicon system including the SVX II cooling bulkheads and ISL support structure.

track reconstruction in three dimensions. The impact parameter resolution of the combination of SVX II and ISL is 40μm including a 30μm contribution from the beamline. The Z_0, primary interaction vertex in the beam direction, resolution of the SVX II and ISL is 70μm.

The 3.1m long cylinderical drift chamber, Central Outer Tracker (COT), covers the radial range from 40 to 137cm and provides 96 measurement layers, organized into alternating axial and $\pm 2°$ stereo superlayers. The COT provides coverage for $|\eta| < 1$. The hit position resolution is approximately 140μm and the momentum resolution is $\sigma(P_T)/P_T^2 = 0.0015$ (GeV/c)$^{-1}$. The COT provides in addition dE/dx, energy loss in detector material, information for the tracks.
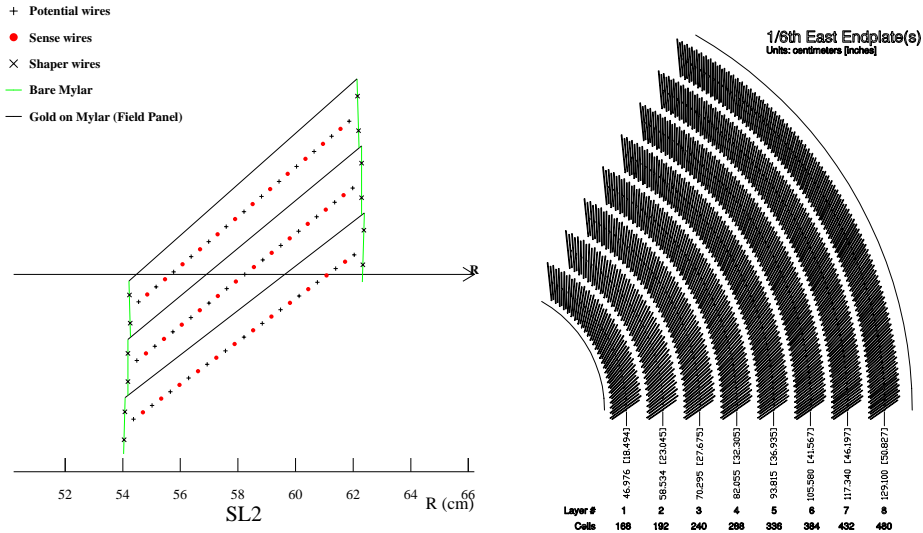
Figure 2.5: (Left) Nominal cell layout for SL2. Other superlayers — including stereo — are similar except for the taper. (Right) 1/6th view of COT east end-plate

2.2.2 Calorimeter

Outside the solenoid, scintillator-based calorimetry covers the region $|\eta| < 3.0$ with separate electromagnetic and hadronic measurements. The CDF calorimeters measure electron and photon energies, jet energies, and net transverse energy flow.

The central calorimeters (and the endwall hadronic calorimeter) cover the pseudo-rapidity range $|\eta| < 1.1(1.3)$ and the plug calorimeters cover $1.1 < |\eta| < 3.64$. It is a scintillator sampling system with tower segmentation: each tower is 15° in azimuth by about 0.11 in pseudo-rapidity. As seen in Figure 2.6, the calorimeter consists of an electromagnetic (EM)

19

section followed by a hadronic (HAD) section. The EM sections are all lead/scintillator sampling and the hadronic sections are iron/scintillator sampling. In both sections the active elements are scintillator tiles read
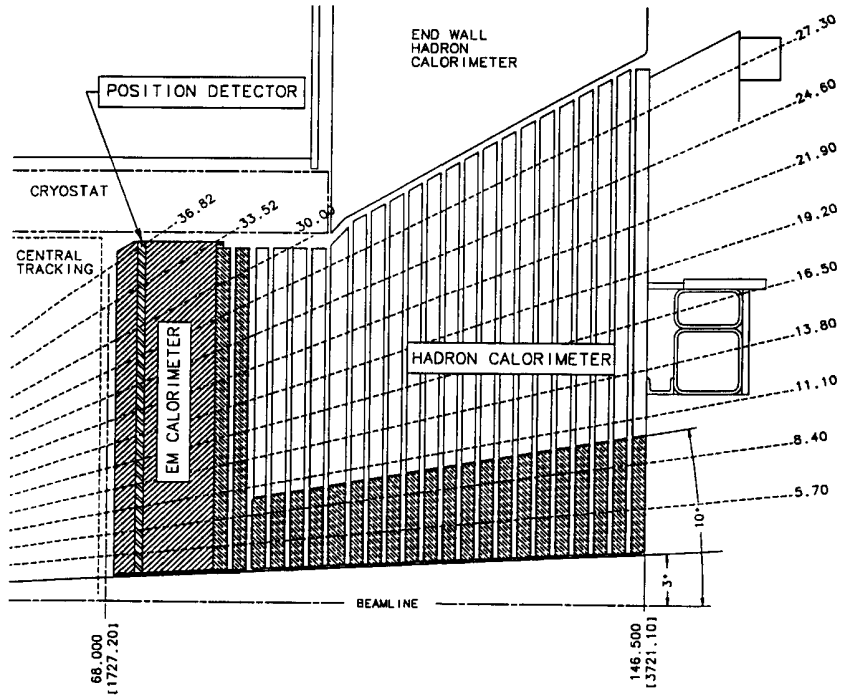
Figure 2.6: Schematic of Towers of the Forward Calorimeter

out by wavelength shifting (WLS) fibers embedded in the scintillator. The WLS fibers are spliced to clear fibers, which carry the light out to photomultiplier tubes (PMT) located on the back plane of each endplug. The EM calorimeter is a lead/scintillator sampling device with a unit layer composed of 4.5mm thick lead and 4mm scintillator. There are 23 layers in depth for

20

a total thickness of about 21 X_0 (radiation lengths) at normal incidence. The detecting elements are arranged in a tower geometry pointing back towards the interaction region. The energy resolution of the EM section is approximately $16\%/\sqrt{E}$ with 1% constant term. The scintillator tiles of the first layer of the EM section are made of 10mm thick scintillator and are read out by multi-anode photomultipliers (MAPMTs). They act as a pre-shower detector. A position detector is located at the depth of the EM shower maximum and is made of scintillator strips read out by WLS fibers.

The hadron calorimeter is a 23 layer iron/scintillator sampling device with a unit layer composed of 50mm iron and 6mm scintillator. The existing iron of the CDF endplugs is used in the hadron calorimeter: stainless steel disks are attached to the inner $10°$ cone to extend the coverage to $3°$. Two additional stainless steel disks are added behind the electromagnetic section to increase the thickness of the hadron calorimeter. The energy resolution of the hadronic calorimeter is $74\%/\sqrt{E}$ with 1% constant term.

2.2.3   Muon Detector

The muon system resides outside the calorimetry. Four layers of plannar drift chambers, the Central Muon detector (CMU), detect muons with $P_T > 1.4$ GeV/c which penetrate the five absorption lengths of calorimeter steel. An additional four layers of plannar drift chambers, the Central Muon Upgrade detector (CMP), instrument 0.6m of steel outside the

magnet return yoke and detect muons with $P_T > 2.0$ GeV/c. The CMU
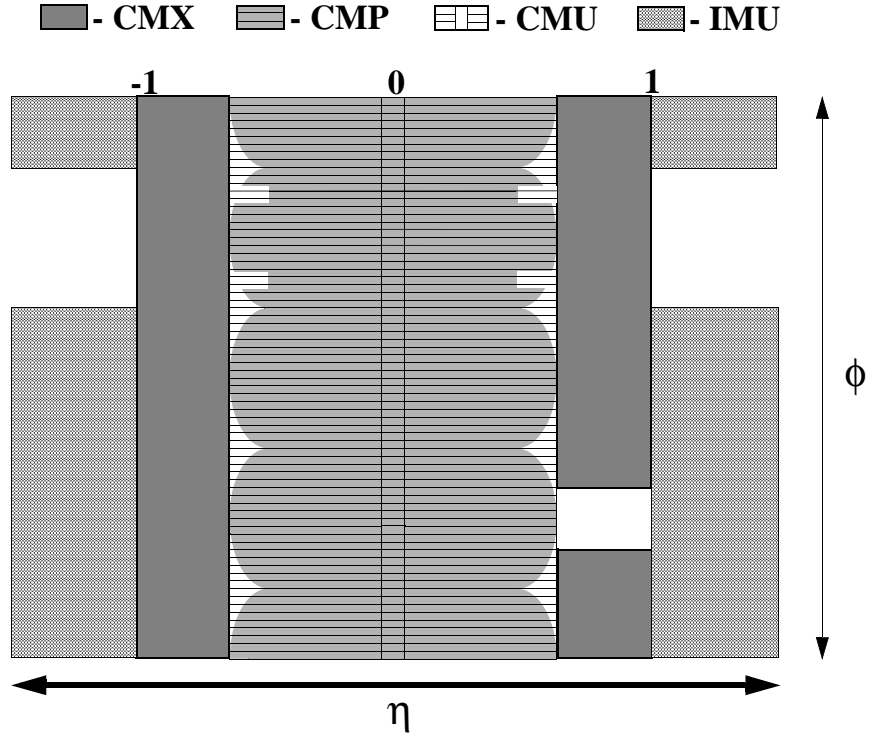
Figure 2.7: The muon components coverage in azimuth ϕ and pseudo-rapidity η.

and CMP chambers each provide coverage in the pseudo-rapidity range $|\eta| < 0.6$. The Central Muon Extention detector (CMX) covers the range $0.6 < |\eta| < 1.0$. The Intermediate MUon detectors (IMU) are covering the region $1.0 < |\eta| < 1.5$. The IMU provide coverage sufficient to identify isolated high P_T tracks as muons or hadrons. The IMU consists of a barrel of drift chambers and scintillation counters around the toroid steel, with additional counters between the toroids and on the endwall to provide

additional projectivity at the trigger level. The IMU counters are virtually identical to the existing central muon detectors and use the same readout electronics.

2.2.4 Trigger System

The trigger and data acquisition systems are designed to accommodate the high rates and large data volume of Run II.

Figure 2.8 shows the functional block diagram of the readout electronics. To accommodate a 132 ns bunch-crossing time and a 4μs decision time for the first trigger level, all front-end electronics are fully pipelined, with on board buffering for 42 beam crossings. Data from the calorimeters, the central tracking chamber, and the muon detectors are sent to the Level 1 trigger system, which determines whether a $p\bar{p}$ collision is sufficiently interesting to hold the data for the Level 2 trigger hardware. The Level 1 trigger is a synchronous system with a decision reaching each front-end card at the end of the 42-crossing pipeline. Upon a Level 1 trigger accept, the data on each frontend card are transferred to one of four local Level 2 buffers. The second trigger level is an asynchronous system with an average decision time of 20μs. Data are collected in DAQ (Data Acquistion system) buffers and then transferred via a network switch to a Level 3 CPU node, where the complete event is assembled, analyzed, and, if accepted, written out to permanent storage.

Dataflow of CDF "Deadtimeless"
Trigger and DAQ

Detector

7.6 MHz Crossing rate
132 ns clock cycle

L1 Storage
Pipeline:
42 Clock
Cycles Deep

L1 trigger

Level1:
7.6 MHz Synchronous pipeline
5544ns latency
<50 kHz Accept rate

L1 Accept

L2 Buffers:
4 Events

L2 trigger

Level 2:
Asynchronous 2 stage pipeline
~20μs latency
300 Hz Accept Rate

L2 Accept

L1+L2 rejection: 20,000:1

DAQ Buffers

L3 Farm

Mass
Storage

PJW 10/28/96

Figure 2.8: Functional block diagram of the CDF II data flow.

CDF II uses a tiered "deadtimeless" trigger architecture. An event is considered sequentially at three levels of approximation, with each level providing sufficient rate reduction for the next level to have minimal deadtime. Level 1 and Level 2 use custom hardware on a limited subset of the data and Level 3 uses a processor farm running on the full event readout. The trigger, like the DAQ, is fully pipelined. The block diagram for the CDF II trigger system is presented in Figure 2.9. Events accepted by the

24

RUN II TRIGGER SYSTEM
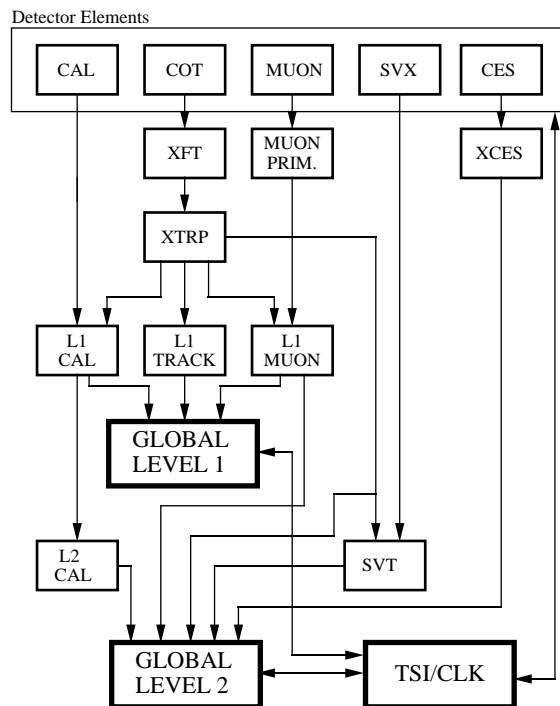
Figure 2.9: Block diagram of the CDF II trigger system.

Level 1 system are processed by the Level 2 hardware. The Silicon Vertex Tracker (SVT) provides the ability to trigger on tracks with large impact parameters. The Level 2 system has improved momentum resolution for tracks, finer angular matching between muon stubs and central tracks, and data from the central shower-max detector (CES) for improved identification of electrons and photons. Jet reconstruction is provided by the Level 2 cluster finder. The output of the first level of the trigger is used to limit

the rate for accepted events to roughly 18 kHz at the luminosity range of $3 - 7 \times 10^{31} \mathrm{cm}^{-2} \mathrm{s}^{-1}$. At the next trigger stage, the rate is reduced further to around 300 Hz. The third and final level of the trigger, with access to the complete event information, uses software algorithms and a computing farm, and reduces the output rate to around 75 Hz, which is written to permanent storage.

CHAPTER III

Data Sample

The data sample for the $W' \to e\nu$ search are selected based on high transverse momentum (P_T) electron or missing transverse energy ($\not{E}_T$) from ν (see Chapter IV) of the final state particles. Having chosen four triggers which will be described below, the inclusive electron sample are collected from the events to have fired one of those triggers at least. The detailed requirements of each trigger path are following.

3.1 Triggers

ELECTRON_CENTRAL_18

- Level 1: L1_CEM8_PT8

  It requires transverse energy in central electromagnetic (EM) cluster greater than 8 GeV and $E_{had}/E_{em} < 0.125$[1]. An XFT(eXtremely Fast Tracker) track pointing to the EM cluster with $P_T > 8$ GeV/c are

---

[1]the electron identification variables are discussed in Section 4.1.1

required.

- Level 2: L2_CEM16_PT8

  A central EM cluster with $E_T^{EM} > 16$ GeV/c and $E_{had}/E_{em} < 0.125$ is required. An XFT track with $P_T > 8$ GeV/c is matched pointing to the cluster

- Level 3: L3_CENTRAL_ELECTRON_18

  A central EM cluster with $E_T^{EM} > 18$ GeV/c and $E_{had}/E_{em} < 0.125$ is required. A COT track is required to be found by the XFT, which also pointing the seed tower of the EM cluster, requires $P_T > 9$ GeV/c.

ELECTRON_70

- Level 1: L1_JET10

  A jet (EM + HAD) cluster is required with $E_T > 10$ GeV/c.

- Level 2: L2_JET90

  A jet cluster with $E_T > 90$ GeV/c is required.

- Level 3: L3_ELECTRON70_CENTRAL

  A central EM cluster with $E_T > 70$ GeV/c is required and a matching COT track momentum should be $P_T > 15$ GeV/c.

W_NOTRACK

- Level 1: L1_EM8_&_MET15

An EM cluster with $E_T^{EM} > 8$ GeV/c and $E_{had}/E_{em} < 0.125$ are required in central or plug electromagnetic calorimeter satisfing with $\not{E}_T > 15$ GeV/c.

- Level 2: L2_CEM16_L1_MET15

  A central EM cluster with $E_T > 16$ GeV/c is required to have the ratio $E_{had}/E_{em} < 0.125$ and $\not{E}_T > 15$ GeV/c.

- Level 3: L3_W_NOTRACK_MET25

  A central or plug cluster has cut the values with $E_T^{EM} > 25$ GeV/c and the ratio $E_{had}/E_{em} < 0.125$. The missing transverse energy cut is $\not{E}_T > 25$ GeV/c.

Z_NOTRACK

- Level 1: L1_EM8

  Two electron candidates from central or plug calorimeter are required with $E_T^{EM} > 8$ GeV/c and $E_{had}/E_{em} < 0.125$.

- Level 2: L2_TWO_EM16

  Two EM clusters $E_T^{EM} > 16$ GeV/c have changed from Level 1.

- Level 3: L3_TWO_ELECTRON18

  Two central or plug electron candidates are required to be greater than 18 GeV/c of E_T^{EM} and the ratio E_{had}/E_{em} be less than 0.125.

EM E_T (GeV)	> 18.0	> 70.0
P_T(GeV/c)	> 9	> 15
E_{had}/E_{em}	< 0.125	No cut
L_{shr}Trk	< 0.2	No cut
E/P	< 4	No cut
ΔX (cm)	< 3 cm	< 3 cm
ΔZ (cm)	< 5 cm	< 5 cm

Table 3.1: Stripping cuts for the inclusive central electrons.

EM E_T (GeV)	> 20.0
E_{had}/E_{em}	< 0.1 or EM E_T > 100 GeV
Iso	< 0.1

Table 3.2: Stripping cuts for inclusive plug electrons.

3.2   Dataset

The inclusive high P_T electron dataset is created after passing the triggers described in Section 3.1. (dataset ID: bhel08/09, 4.8.4 production)

The inclusive electron sample has been stripped again (see Tables 3.1 and 3.2 for the definition) and also reprocessed in cdfsoft2 version 4.11.1 (dataset ID: rtop0c, 4.11.1 REMAKE Inclusive electrons).

In order to select good electrons, the good run list [15] in CDF database check the status of each detector component during data taking. Since beam constrained COT only track[2] is used in this analysis, we don't require for the silicon.

Finally the corresponding integrated luminosity is 205 ± 12 pb^{-1} after applying good run requirements and the run number ranges are between

---

[2]The raw COT resolution can be improved by imposing the track fit through beam spot. All the tracks in this analysis have been beam constrained COT only tracks
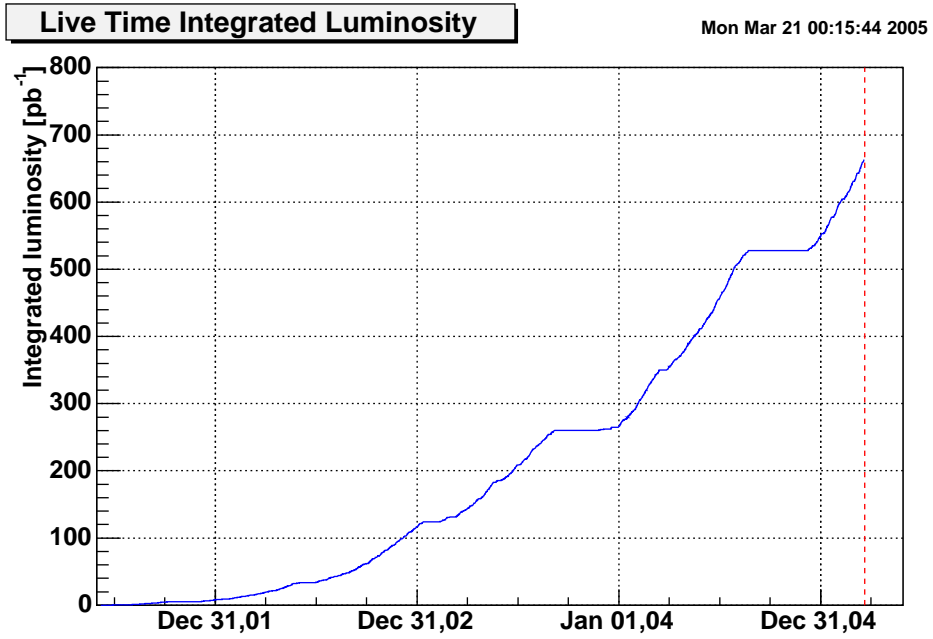
Figure 3.1: Live integrated Lum vs time

141544 and 168889 of the data obtained from february 2002 to september 2003 (see Figure 3.1). Remaining events after all the requirements are $\sim 4.6 \times 10^6$ events.

CHAPTER IV

Event Candidate Selection

The W' boson searches in this analysis are performed by finding decaying to an electron and neutrino pair in the final state. The identified high E_T electron of four-momentum is measured in the calorimeter and the neutrino can be detected by calculating missing transverse energy which can be derived from the momentum balance of all deposited energy in calorimeter since the longitudinal momentum of the neutrino to the beam cannot be measured at the $p\bar{p}$ collider. The W' boson is reconstructed in the transverse mass (M_T) distribution

$$(4.1) \qquad M_T = \sqrt{2E_T^e \, \not{E}_T \left(1 - cos\phi_{e\nu}\right)}$$

where E_T^e $(\not{E}_T)$ is the transverse energy of the electron (neutrino) and $\phi_{e\nu}$ is the azimuthal angle between the electron candidate and the $\not{E}_T$ direction. The production of a W' boson decaying to an electron-neutrino pair would be expected as an excess or a bump above the standard model background

in the M_T distribution.

4.1 Basic Signal Cut for the $W/W' \to e\nu$ Sample

The electron events have been selected with cuts designed to remain very
efficient for high E_T electrons. Primary, the highest E_T, electron candidates
were required to be in a fiducial region of the central EM calorimeter with
$E_T > 25$ GeV and the neutrino transverse energy by requiring to be $\not{E}_T >$
25 GeV. Following two sections describe the electron identification and how
to calculate missing transverse energy.

4.1.1 Central Electron Identification Variables

Table 4.1 shows the electron identification cut values. The definition of
the central electron cut variables are:

- E_{had}/E_{em} is the ratio of the hadronic energy to the electromagnetic
  energy in all towers included in the cluster.

- E/P is the ratio of the electron energy to the momentum of the highest
  P_T COT track pointing to the cluster.

- Iso is a variable defined as

(4.2)
$$Iso = \frac{E_T^{0.4} - E_T^e}{E_T^e},$$

where $E_T^{0.4}$ is the transverse energy deposited in the cone of $R =$

$\sqrt{(\Delta\phi)^2 + (\Delta\eta)^2}$ and E_T^e is the transvserse energy of the electron candidate.

- Δx is the difference between COT track position extrapolated to CES and the position measured with CES in the $r - \phi$ view.

- Δz is the difference between COT track position extrapolated to CES and the position measured with CES in z view.

- L_{shr} is a variable that can be used to compare the lateral shower profiles of electrons between data and expected in the calorimeter towers. It is defined as

$$(4.3) \qquad L_{shr} = 0.14 \sum_i \frac{E_i^{adj} - E_i^{prob}}{\sqrt{0.14^2 E + (\Delta E_i^{prob})^2}},$$

where E_T^{adj} is the measured energy in a tower neighbouring the seed tower, E_T^{prob} is the expected energy in the same tower, $0.14^2 E$ is the uncertainty on the energy measurement, and ΔE_i^{prob} is the uncertainty in E_i^{prob}. The E_i^{prob} is calculated with the testbeam data.

- FIDELE is a variable to avoid inactive detector region using CES local coordinate.

$$(4.4) \qquad\qquad -21cm < X_{CES} < 21cm$$

$$(4.5) \qquad\qquad 9cm < Z_{CES} < 230cm$$

ID Variables	central	plug
E_T	> 25 GeV (> 15 GeV)	> 15 GeV
P_T	> 15 GeV/c	
Iso	< 0.2	< 0.1
E_{had}/E_{em}	$< 0.055 + 0.00045 \times E$	$< 0.055 + 0.00045 \times E$
E/P	< 4 (if $E_T < 100$ GeV)	
Δx	< 3.0 cm	
Δz	< 5.0 cm	
L_{shr}	< 0.2	
$\chi^2_{3\times3}$		< 10
$|Z_0|$	< 60.0 cm	
FIDELE	$= 1$ (Fiducial in CEM)	$1 < |\eta| < 3$

Table 4.1: Electron identification cuts for $W/W' \rightarrow e\nu$ selection. The $E_T > 15$ GeV cut on the central electron candidate is the requirement for the secondary highest E_T electron to be used for the dilepton event removal cut.

4.1.2 Missing Transverse Energy

The $\not{E}_T$ is calculated from all of the calorimeter towers in central and plug. The towers are required to be greater than 0.1 GeV energy. The $\not{E}_T$ is corrected for muons with P_T of the track pointing calorimeter and recalculated for the primary vertex of the event by the jet vertex algorithm. The $\not{E}_T$ mismeasurement mainly depends on mismeasurement in jet energy from calorimeter nonlinearity and loss in cracks and dead zones. Here, an additional correction for the $\not{E}_T$ has been given, that is, a requirement of level 5 correction in Run II jet energy correction [16]. As described in Ref. [17], the contents applied are following:

- Relative energy corrections to make the calorimeter response uniform in η (determined from data)

- Time dependence corrections

- Raw energy scale corrections

- Multiple Interaction corrections

- Absolute energy corrections to convert calorimeter cluster P_T to the sum of the P_T of the particles in the cone (use calorimeter calibration and jet fragmentation properties, as well as simulation tuned to test beam and $p\bar{p}$ data)

The corrected missing transverse energy is calculated as the negative vector sum of the transverse energy of the corrected jet energy in the towers

$$(4.6) \qquad \vec{\not{E}}_T^{\,corr} \equiv - \sum_{i=tower} \vec{E}_{T_i}^{corr}$$

where $\vec{E}_{T_i}^{corr}$ is vector sum of the corrected transverse energy over calorimeter towers. The resolution of the $\not{E}_T$ is measured to be ~ 5 GeV at the W event kinematic region.

4.2 Dilepton Event Removal

Addtionally, dilepion events coming from Drell-Yan, $t\bar{t}$, and diboson backgrounds were removed. For the secondary electron, we select the electron E_T greater than 15 GeV in central or plug region. The identificaion cuts are listed in Table 4.1. In the case of the muon, its track P_T is required to be greater than 15 GeV. The muon selection criteria are listed in Table 4.2.

ID Variables	
P_T	> 15 GeV/c
E_{em}	< 2 (if $P < 100$GeV/c)
	$< 2 + 0.0115 \times (P - 100)$ (if $P > 100$GeV/c)
E_{had}	< 6 (if $P < 100$GeV/c)
	$< 6 + 0.0280 \times (P - 100)$ (if $P > 100$GeV/c)
ΔX(CMU)	< 3 cm
ΔX(CMP)	< 5 cm
ΔX(CMX)	< 6 cm

Table 4.2: Muon identification cuts for dilepton removal.

All these lepton identificaion cut values are selected based on the analyses for the searches of $Z' \rightarrow ee$ [18] and $Z' \rightarrow \mu\mu$ [19]. We remove events with an additional lepton that passes either the secondary lepton identification cuts.

4.3   Multijet Event Removal ($E_T/\not{E}_T$ Cut)

The multijet events end up in the $W/W' \rightarrow e\nu$ sample when one of the jets is misidentified as an electron and the missing energy from the vector sum of the transverse energy in the event satisfies $\not{E}_T > 25$ GeV. In this case, the electron candidate E_T and $\not{E}_T$ will less likely be comparable in magnitude, whereas a $W' \rightarrow e\nu$ event will have an electron and a neutrino going opposite direction with comparable magnitude in E_T and $\not{E}_T$, respectively, if P_T of the boson is much smaller than the mass of the boson.

Shown in Figure 4.1 are the E_T vs $\not{E}_T$ distributions using Monte Carlo samples of $W \rightarrow e\nu$, $W' \rightarrow e\nu$ of $M_{W'} = 250$, 500, and 750 GeV/c^2 (see

Section 6.3 for the description). Most events lie on $E_T/\not{E}_T \sim 1$ regardless of the mass of the boson. We require the candidate events to satisfy $0.4 < E_T/\not{E}_T < 2.5$. The events that lie outside the allowed region mostly have high boson P_T or mismeasured E_T or $\not{E}_T$. When a W boson is boosted to electron or neutrino direction in ϕ, the event is likely to end up outside the allowed region, as evidenced in the $W \rightarrow e\nu$ distribution. A much heavier W' boson with both electron E_T and $\not{E}_T$ comparably larger than the boson P_T would much less likely to be outside the allowed region. The efficiency of the cut on $W/W' \rightarrow e\nu$ is calculated to be > 0.99. In the case of multijet, the cut is not efficient in removing multijet events in the low M_T region. However, it becomes efficient in the high M_T region. The rejection rate above $M_T = 100$ GeV/c^2 is $\sim 40\%$ in the multijet enriched sample shown in Figure 4.2.

Figure 4.2 shows the E_T vs $\not{E}_T$ distribution of the multijet enriched sample which will be discussed in Section 7.2. Majority of events failing the ratio cut have large $E_T/\not{E}_T$ values. This is due to the fact that $\not{E}_T$ is coming from mismeasured E_T of electron candidates which are mostly jets.

4.4 Final Event Sample and Transverse Mass Distribution

Figure 4.3 shows electron E_T and $\not{E}_T$ distributions from data after all the event selection cuts for the $W/W' \rightarrow e\nu$ sample. There were 1.2×10^6 events remained. The resulting M_T distribution is shown in Figure 4.4. The
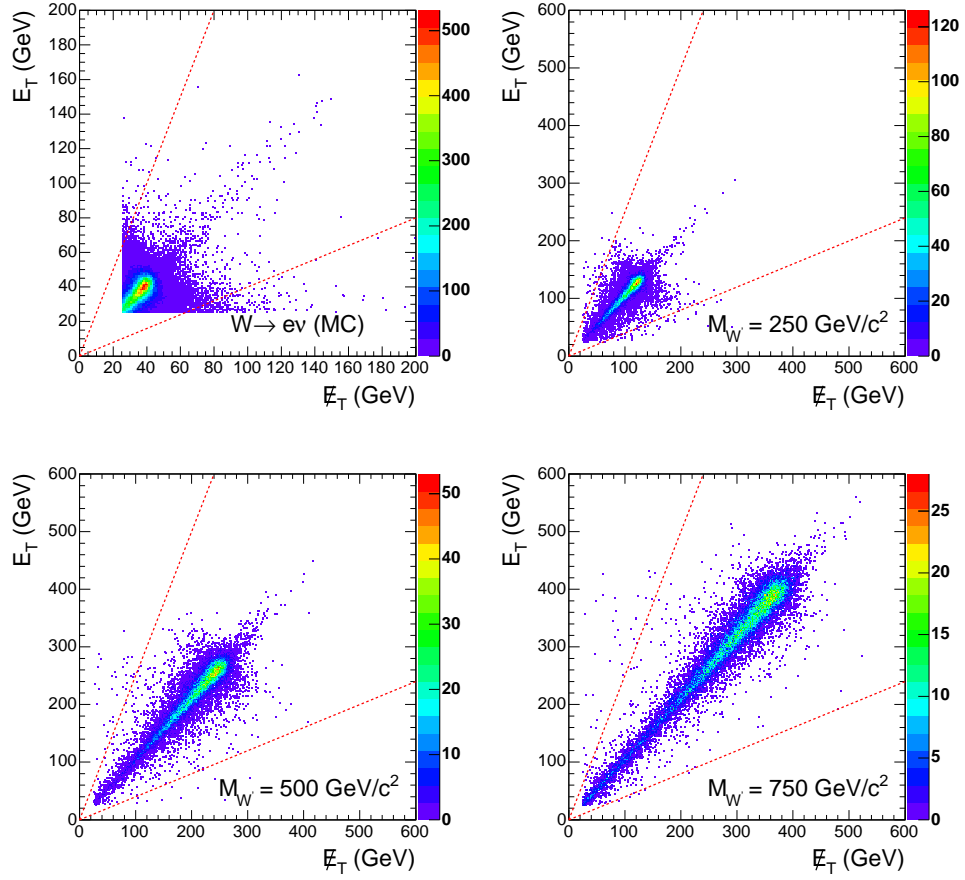
Figure 4.1: The electron E_T vs $\not{E}_T$ distributions in Monte Carlo samples of $W \to e\nu$ (top left), $W' \to e\nu$ of 250 GeV/c^2 (top right), 500 GeV/c^2 (bottom left), and 750 GeV/c^2 (bottom right). The dashed lines are the boundaries on $E_T/\not{E}_T$ cut $(0.4 < E_T/\not{E}_T < 2.5)$.

39
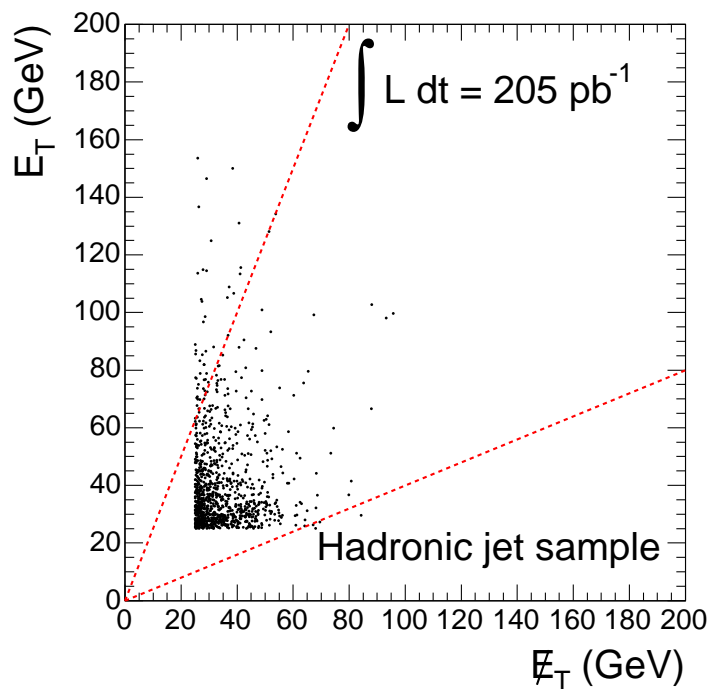
Figure 4.2: The electron candidate E_T *vs* $\not{E}_T$ distributions of the multijet enriched sample in Section 7.2. The electron candidate E_T is corrected to compensate for the non-isolated electron candidates. The dashed lines are the boundaries on $E_T/\not{E}_T$ cut $(0.4 < E_T/\not{E}_T < 2.5)$.
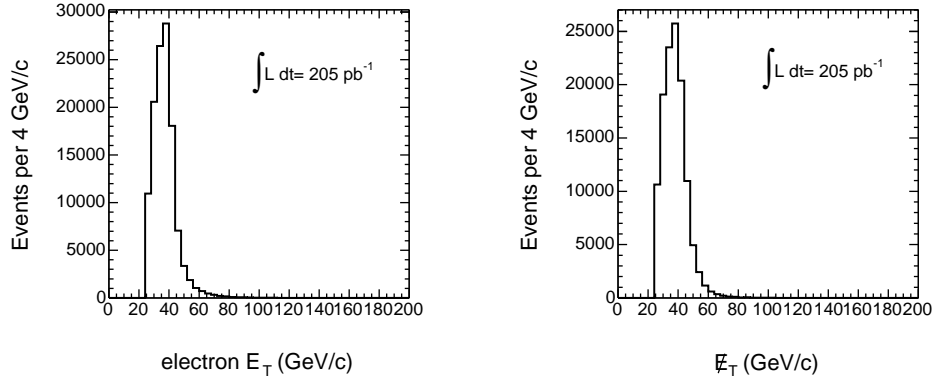
Figure 4.3: Central electron E_T (left) and $\not{E}_T$ distribution (right) after applying event selection cuts in data sample.

highest M_T event with $M_T = 524$ GeV/c^2 is shown in event display view in Figure 4.5.
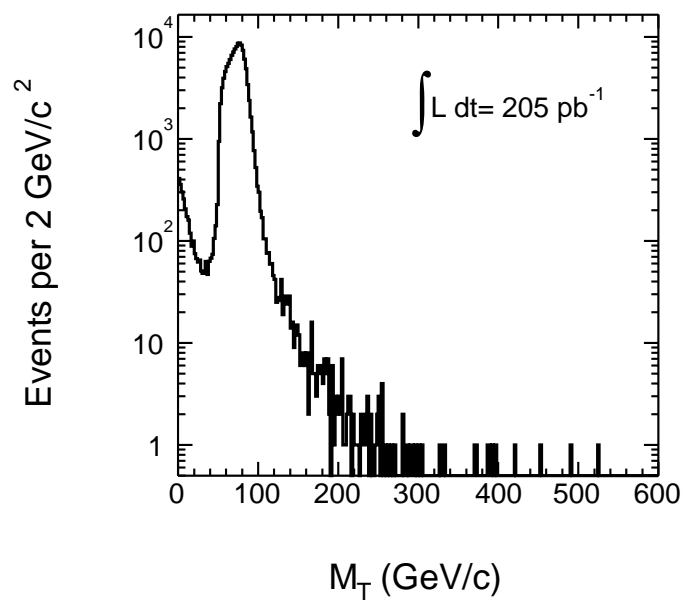
Figure 4.4: The transverse mass distribution after the event selection.

Missing Et
Et=251.5 phi=5.1

List of Tracks
Id   pt   phi   eta

Cdf Tracks: first 5
418 -334.8 2.0 -0.7
459   2.9 -0.4 0.8
460   -1.7   2.9 0.0
461   1.5 -0.5 -1.2
438   1.5   2.8 -0.1

To select track type
SelectCdfTrack(Id)

Svt Tracks: first 5
  0   90.4 2.0

To select track type
SelectSvtTrack(Id)

Et = 244.90 GeV

Particles: first 5
pdg   pt   phi eta
 11   334.8   2.0 -0.7
To list all particles
ListCdfParticles()

Jets(R = 0.7): first 5
Em/Tot et   phi eta
 0.9   246.1 2.0 -0.9
To list all jets
ListCdfJets()

Figure 4.5:   The event display view of the highest M_T event with $M_T = 524$ GeV/c^2.

43

CHAPTER V

Central Electron Efficiencies

In determining the expected number of $W' \to e\nu$ signal events in the $W/W' \to e\nu$ event candidate sample, the efficiencies are accounted for event selection including triggers, and the kinematic and geometric acceptances of the events. This chapter shows the measured efficiencies of the triggers and the central electron selections. However, later in the likelihood fit method of the M_T distributions (in Chapter VIII), the standard model backgrounds and the signal are renormalized by the factor α_0, the overall normalization, thus any discrepancy between the actual trigger efficiency and the assumption of 100% efficiency (mentioned in Section 7.1), as well as the electron selection cut, is absorbed by α_0.

5.1 Trigger Efficiencies

The high E_T electron triggers as described in Section 3.1 include track triggers, involving the XFT at Level 1 and Level 2 and the COT at Level 3,

and calorimeter triggers at Level 1, Level 2 and Level 3. The efficiency of the triggers are calculated at each step of these detector components. The XFT and COT tracking efficiencies have been calculated using the W_NOTRACK trigger, where the same calorimeter requirements were used for the high E_T electron trigger but does not require tracks associated with the EM clusters. The track triggers' efficiencies are measured to be independent of P_T for tracks with $P_T > 10$ GeV/c, but dependent on η for the Level 1 and Level 3 triggers. The Level 2 track triggers are 100% efficient. The Level 1 calorimeter trigger has been studied using a sample of inclusive muons and removing any activity in the plug. The Level 1 and Level 3 calorimeter trigger efficiency for electrons with $E_T > 20$ GeV is estimated to be 100%. As the Level 1 and Level 3 calorimeter triggers are fully efficient, the electron trigger efficiency is determined in the tracking trigger efficiency ending up to be $96.8 \pm 0.1\%$ [20].

In ELECTRON_CENTRAL_18 trigger, the effect of E_{had}/E_{em} cut has been studied on an electron of the ELECTRON_CENTRAL_18 trigger using single electron Monte Carlo data sample [21]. In this result, it has been found that there were the saturation of Level 2 read-out electronics at around 128 GeV in an EM tower from the Level 2 cluster E_T distribution and that 12.5% of Level 2 for E_{had}/E_{em} cut is significantly less efficient for very high E_T electrons (>150 GeV). The ELECTRON_70 trigger is more

ID Variables	Tight cluster	Central cluster
E_T	> 25 GeV	> 25 GeV
trkP_T	> 15 GeV/c	> 15GeV/c
η	$< 1.1(CEM)$	$< 1.1(CEM)$
FIDELE	$= 1$ (Fiducial in CEM)	$= 1$ (Fiducial in CEM)
$|Z_0|$	< 60.0 cm	< 60.0 cm
Iso	< 0.2	
E_{had}/E_{em}	$< 0.055 + 0.00045 \times E$	
E/P	< 4 (if $E_T < 100$ GeV)	
Δx	< 3.0 cm	
Δz	< 5.0 cm	
L_{shr}	< 0.2	

Table 5.1: A sample of $Z \rightarrow e^+e^-$ (data) to be used to calculate the electron selection efficiency. The mass range has been selected with ($70 < M_{e^+e^-} < 110$GeV/c^2) to reduce the number of background events in the sample.

efficient for high E_T with no E_{had}/E_{em} requirement. Front-end electronics of calorimeter has a good scale for the input charge of 1300 pC, this corresponds to be ~ 800 GeV. For the offline reconstruction, there is no saturation up to ~ 800 GeV. Combining the effect from all the triggers, the overall efficiencies for high E_T electron appears to be $\sim 100\%$ efficient.

5.2   Electron Selection Efficiencies

In order to measure the efficiencies of the electron selection cuts, a sample of $Z \rightarrow e^+e^-$ data was used. The sample was made with a tight electron requirement on one electron leg and a loose electron requirement on a second EM cluster for the other leg, both in the central region. The invariant mass of the electron and the EM cluster was required to be $70 < M_{e^+e^-} < 110$GeV/c^2. See Table 5.1 for the cuts applied on electrons.

The i-th electron identification variable efficiency is calculated as,

$$(5.1) \qquad \epsilon^i = \frac{N_{Ti} + N_{TT}}{N_{CC} + N_{TT}}$$

where N_{TT} is the number of events with both legs passing the tight central electron cuts and N_{CC} is the number of events with one leg passing the tight selection criteria and the other leg passing the cuts for the second central cluster in Table 5.1. N_{Ti} is the number of events satisfing the tight cuts on one leg and the i-th identification cut on the second leg. The same sign events regarded as jet background were subtracted in these numbers of events. The efficiencies of the i-th electron identification variables are summarized in Table 5.2. For the total efficiency by requiring both legs pass the tight cuts, the above formula can be

$$(5.2) \qquad \epsilon_T = \frac{2N_{TT}}{N_{CC} + N_{TT}}$$

where there are 5071 events for N_{CC} and 4631 events for N_{TT} after subtracting jet background in the sample. The calculated total electron selection efficiency (ϵ_T) is 95.5±0.2%. Figure 5.1 (5.2) shows this total (i-th) electron identification efficiency as a function of the E_T.

ID Variables	Number of candidate events	Number of background events	Efficiency(%)
Iso	4963	116	97.7 ± 0.2
E_{had}/E_{em}	4979	127	97.7 ± 0.2
E/P	5355	285	99.9 ± 0.0
Δx	5241	257	99.1 ± 0.1
Δz	5292	267	99.5 ± 0.1
L_{shr}	5051	156	98.2 ± 0.1
ϵ_T	4698	67	95.5 ± 0.2

Table 5.2: Efficiency ϵ^i for the i-th identification variable and ϵ_T for total applied all the identification cuts. These efficiencies were corrected for same sign events regarded as the jet background.
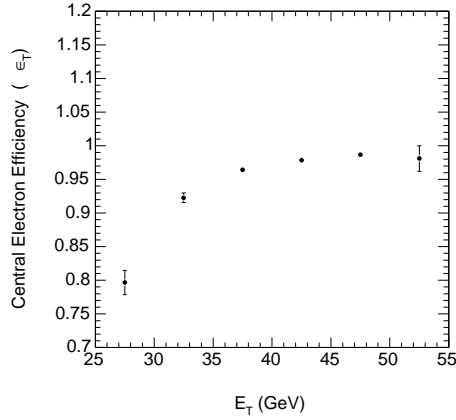
Figure 5.1: Central electron selection efficiency as a function of E_T.
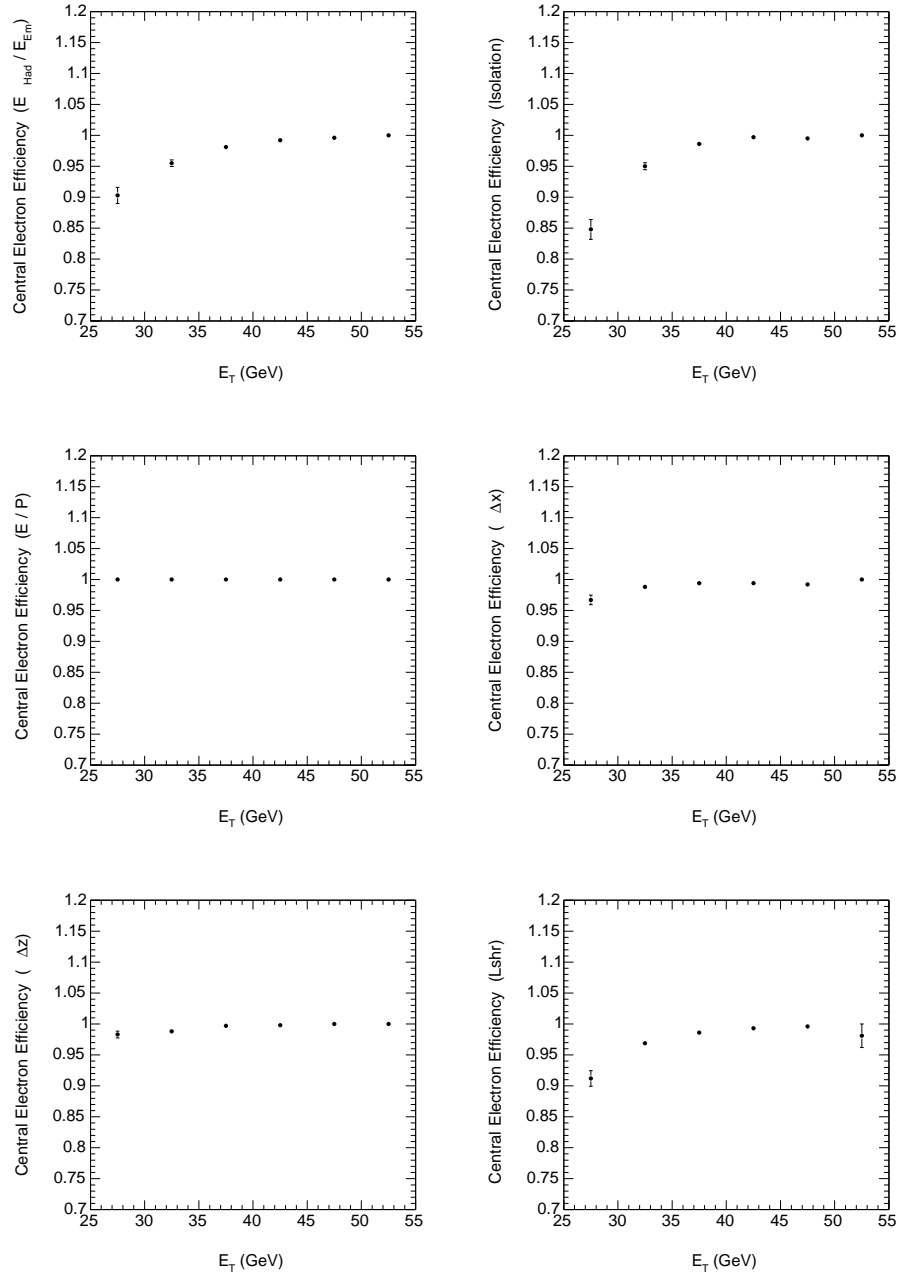
Figure 5.2: Central electron selection efficiencies on each electron variables as a function of E_T.

CHAPTER VI

Monte Carlo

6.1   Electron Energy Scale and Resolution

In this section, the discrepancy in the electron energy response of the calorimeter between data and Monte Carlo (MC) is investigated. The electron energy scale and resolution in MC is compared against data. The discrepancy between the invariant mass values calculated in the data and MC can be written as

$$\delta M = \frac{1}{2} \left(\frac{\delta E_1}{E_1} + \frac{\delta E_2}{E_2} \right) M,$$
(6.1)

where E_1 and E_2 are the energy values of the two electrons in the $Z \rightarrow ee$ events. If we take this discrepancy to be originated from the energy scale differences in the data and MC, we can write Eq. 6.1 as

$$\frac{\delta M}{M} = \alpha(E_1 + E_2)/2 + \beta,$$
(6.2)

assuming the energy scale discrepancy is a linear function, i.e.

$$\frac{\delta E}{E} = \alpha E + \beta.$$
(6.3)

In order to investigate the energy dependence of $\delta E/E$, we divided both data and MC the $Z \to ee$ samples into 12 subsamples of E_1+E_2 region (from 90 to 140 GeV at 5 GeV intervals, $140 \sim 160$ GeV, and $160 \sim 190$ GeV). The invariant mass distributions of a couple of subsamples are shown in Figure 6.1. The distributions are not well fit with a single gaussian function as the cuts on $E_1 + E_2$ skews the distributions. We used a double gaussian to fit the MC distribution first. Assuming the MC distributions describe the data shape well, we fixed the relative fraction and the ratio of the widths of two gaussians and fit the data distribution. Also, the difference in mean was varied as a linear function of the width.

We used the mean of the narrower gaussian to compare the "peak position" in the mass distributions between data and MC.[1] We take the relative difference, (Data-MC)/MC, as a function of E_1+E_2 and fit it with a straight line. The fit results are

(6.4) $\alpha = (6.67 \pm 1.11) \times 10^{-4} \text{ GeV}^{-1}$ and $\beta = (-3.54 \pm 0.56) \times 10^{-2}$

and shown in Figure 6.2.

However, the correction on MC based on this fit results most likely over-correct the electron energy at very high energy region. A recent study with higher statistics sample seems to suggest that the residual shown in Figure 6.2 dies down at high $E_1 + E_2$ region. The esteemed CDF EM calorime-

---

[1]Ideally, one would prefer to use the real peak position of the invariant mass distributions. However, it is enough to find how much a particular feature in the distribution is moved.

ter expert L. Nodulman suggested not to make energy correction since "the X_0 drives the leakage and the CDF Monte Carlo calculations should get it right" [22]. Instead he suggested to take the associated uncertainty to 3% based on the spread in the residual distribution and we followed his suggestion.

The discrepancy in the electron energy resolution between data and MC is also considered. Figure 6.3 shows the width of the narrower gaussian of the double gaussian used to fit the invariant mass distributions as discribed above as a function of the sum of the energy of two electrons. Also shown are the ratio, Data/MC, of the widths.

The width of the invariant mass distribution is

$$(6.5) \qquad \sigma = \sqrt{\frac{1}{4}\left(\left(\frac{\delta E_1}{E_1}\right)^2 + \left(\frac{\delta E_2}{E_2}\right)^2\right)M^2 + \Gamma_Z{}^2},$$

where $\Gamma_Z = 2.5$ GeV/c^2 is the total width of Z. The ratio of the width of the data distribution to that of the MC distribution $R = \sigma_D/\sigma_{MC}$ is, then,

$$(6.6) \qquad R^2 = \frac{\frac{1}{4}((\delta E_{1_D}/E_1)^2 + (\delta E_{2_D}/E_2)^2)M^2 + \Gamma_Z{}^2}{\frac{1}{4}((\delta E_{1_{MC}}/E_1)^2 + (\delta E_{2_{MC}}/E_2)^2)M^2 + \Gamma_Z{}^2}.$$

Approximating $\delta E_1/E_1 = \delta E_2/E_2$ and rearranging Eq. 6.6, we get

$$(6.7) \qquad \left(\frac{\delta E_D}{\delta E_{MC}}\right)^2 = (R^2 - 1)\left(1 + 2\left(\frac{\Gamma_Z/M}{\delta E_{MC}/E}\right)^2\right) + 1.$$

The data distributions are $\sim 10\%$ wider than the MC distributions regardless of $E_1 + E_2$ value, i.e. $R = 1.1$, as shown in Figure 6.3. Assuming
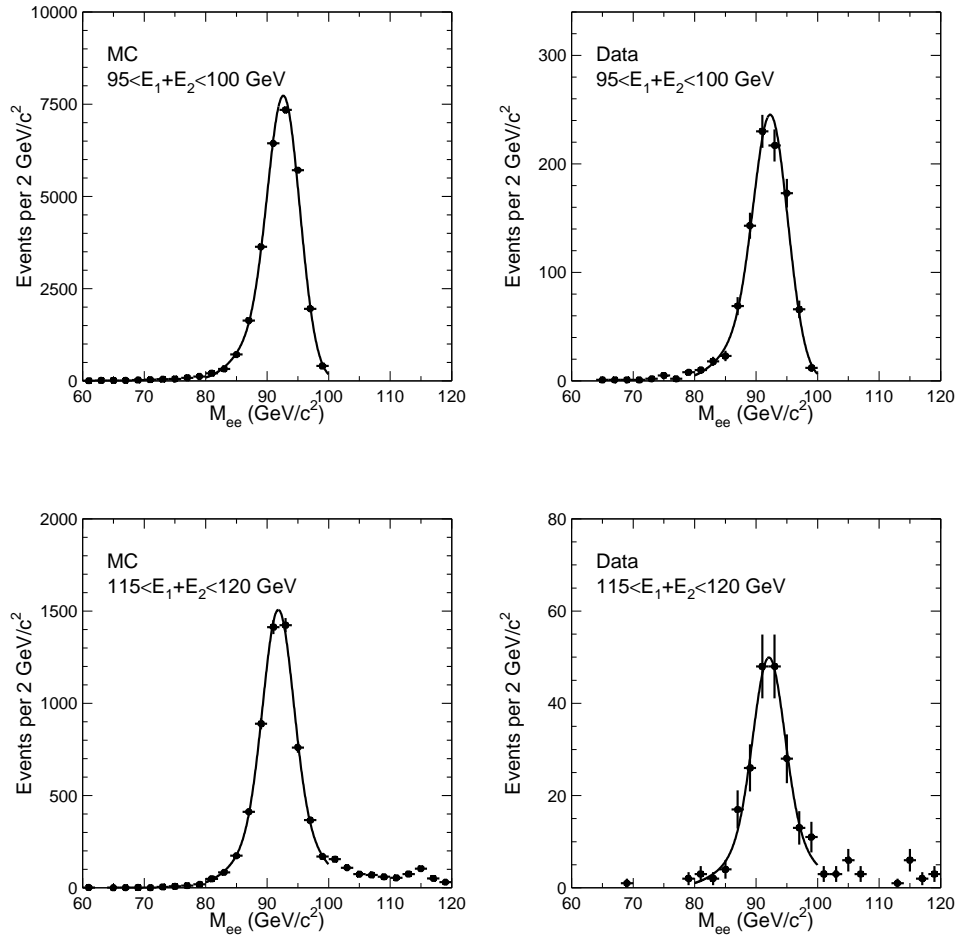
Figure 6.1: Invariant mass distributions of $Z \rightarrow ee$ samples of MC (left) and data (right). The top plots are the subsamples with the sum of two electron energy between 95 and 100 GeV and bottom plots are between 115 and 120 GeV. The solid curves show the fit with a double gaussian function. The details of the fit function and the procedure are described in Section 6.1.

53
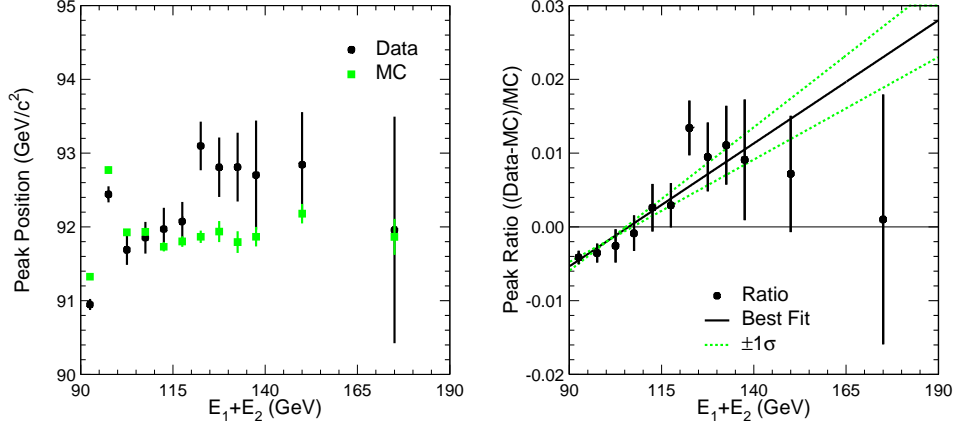
Figure 6.2: The mean of the narrower gaussian of a double gaussian as a function of the sum of two electron energy in $Z \rightarrow ee$ data and MC samples (left) and the ratios of the means of the narrower gaussian with a straight line fit (right).

$\delta E_{MC}/E = 0.13/\sqrt{E}$ and taking $M \simeq 91$ GeV/c^2, using Eq. 6.7 we get ~ 1.5 and ~ 3.0 times larger $\delta E/E$ at $E = 50$ and 400 GeV, respectively, for data than MC, i.e. $0.13/\sqrt{E}$.[2] The electron energy in MC is smeared by Eq. 6.7.[3]

6.2 Background Sample

Backgrounds to $W' \rightarrow e\nu$ production come from sources including real electrons such as,

- $W \rightarrow e\nu$

---

[2]Even if we take $\delta E_{MC}/E = 0.2/\sqrt{E}$, which is closer to what we measure with the invariant mass distribution of $Z \rightarrow ee$ data, the resulting corrected resolution differs by $\sim 10\%$.

[3]The additional smearing factor to E_{MC} is then $\sqrt{(\delta E_D/\delta E_{MC})^2 - 1} \times (\delta E_{MC}/E)$.
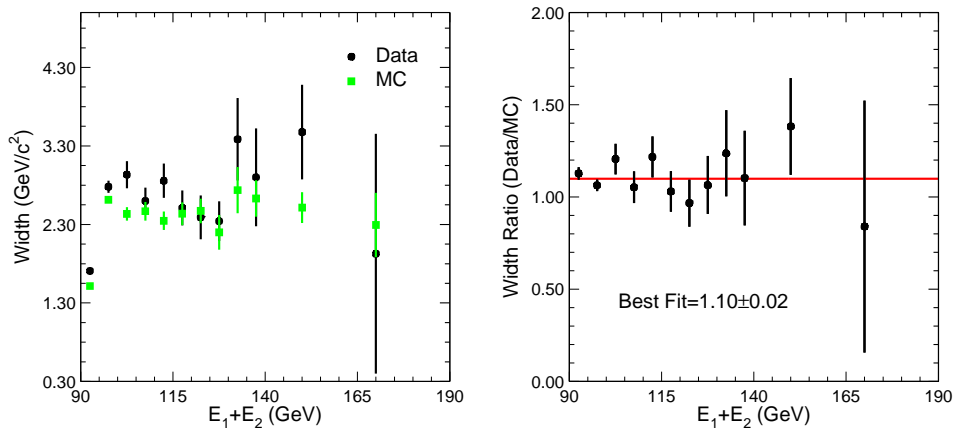
Figure 6.3: The width of the narrower gaussian (left) in the double gaussian function used to fit the invariant mass distributions and the ratio of data to MC (right) as a function of the sum of two electron energy.
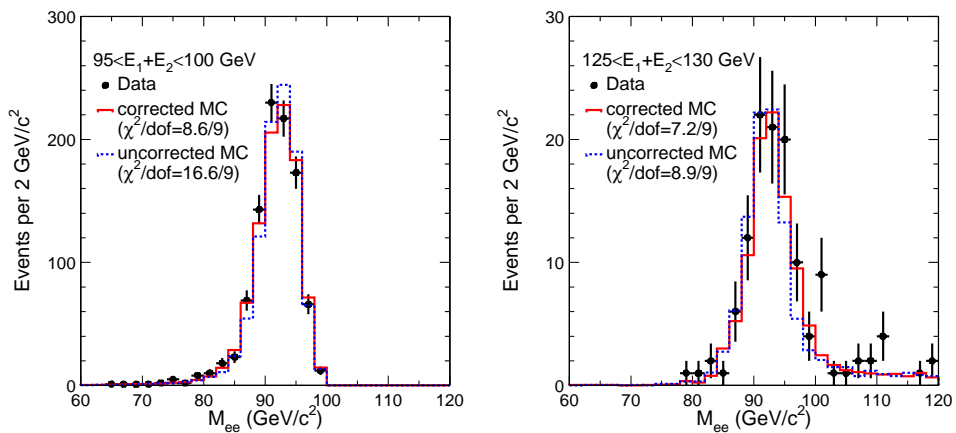
Figure 6.4: The comparison of $Z \rightarrow ee$ invariant mass distributions between data and MC after the electron energy scale and resolution correction. Also shown are the distributions before the correction.

- $W \to \tau\nu \to eX$

- $Z/\gamma \to ee$

- $Z/\gamma \to \tau\tau \to eX$

- $t\bar{t} \to eX$

- Diboson $(WW, WZ) \to eX$

and from multijet background faking electron candidates.

For these backgrounds except for multijet, MC samples are used to estimate and to obtain each shape. The multijet background contribution is calculated using data sample, which will be discussed in Section 7.2 in detail. For the MC samples of backgrounds except diboson, events are generated with PYTHIA [23], using Parton Distribution Function (PDF) of CTEQ5L [24]. These PYTHIA MC samples are tuned to match observed data. Initial and final state radiation were turned on. The beam energy is set to 980 GeV/c^2 and event vertex distribution is set to match the data. A sample of 2,069,739 $W \to e\nu$ events and 273,426 $W \to \tau\nu$ events are generated. A sample of 1,970,444 $Z/\gamma \to ee$ events and 497,415 $Z/\gamma \to \tau\tau$ events are generated with minimum invariant mass of 30 GeV, and 693,589 $t\bar{t}$ events are used for each background calculation. For the WW and WZ sample, 964,868 WW events and 964,868 WZ events are generated using ALPGEN [25] interfaced with HERWIG [26]. The generated events are

then passed through the detector simulation [27] and are reconstructed in the cdfsoft2 version 4.9.1. As for all these backgrounds and signals described in next section, Monte Carlo samples are corrected with electron energy resolution studied in Section 6.1.

6.3 Signal Sample

The $W' \to e\nu$ signal events are generated with PYTHIA using CTEQ5L PDF. It is assumed that the right-handed sector CKM matrix is the same as that of left-handed sector, that is of the standard model [28]. We used $V + A$ couplings but the strength is assumed to be the same as the standard model.[4] Some of the parameters in PYTHIA are tuned to match the boson P_T distribution observed in Run I [29].

The W' boson with mass values of 200 to 950 GeV/c^2 at 50 GeV/c^2 intervals was generated, with $\sim 50\,000$ events at each mass value. The total width and the branching fraction of $W' \to e\nu$ are shown in Figures 1.4 and 1.5.

Since the cross sections calculated in PYTHIA are in leading order (LO), we used the next-to-next-to-leading order (NNLO) calculation code written by R. Hamberg *et al.* [30] using MRST1 PDF set [31]. Table 6.1 shows $\mathcal{B}(W' \to e\nu)$, $\sigma \cdot \mathcal{B}(W' \to e\nu)$, and the expected number of events of W' bosons. Figure 6.5 shows $\sigma(p\bar{p} \to W')$ and $\sigma(p\bar{p} \to W') \cdot \mathcal{B}(W' \to e\nu)$. Also,

---

[4]We will refer this as standard model strength coupling, henceforth.
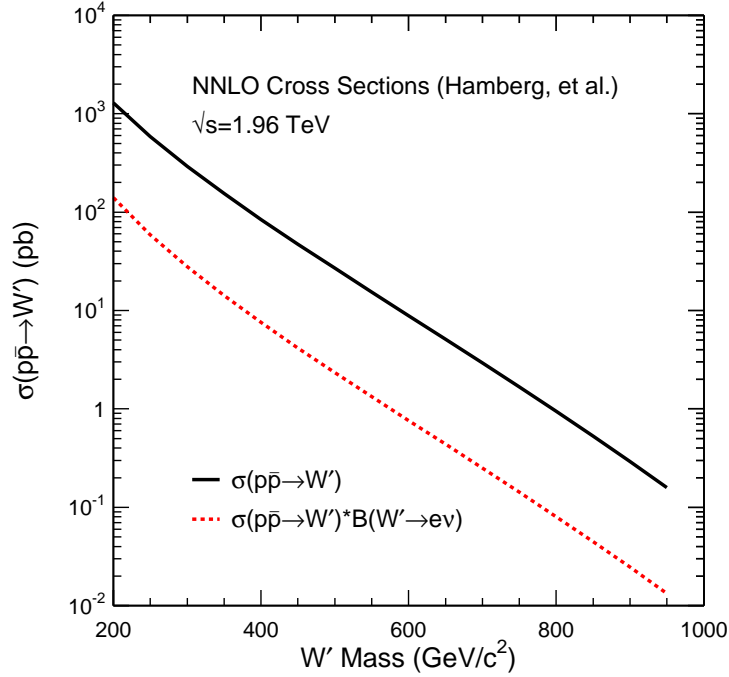
Figure 6.5: Cross section of $p\bar{p} \rightarrow W'$ at $\sqrt{s} = 1.96$ TeV calculated using Ref. [30] with NNLO (MRST1). Also, cross section times branching fraction is shown.

the signal acceptance is shown in Figure 6.6.

The NNLO calculation code provided by L. J. Dixon [32] using MRST4 (NNLO) PDF is used to check the production kinematics of W' boson ($d\sigma/dY$) as well as W boson ($d\sigma/dm$) in PYTHIA and found to be in good agreements in terms of the shapes of the distributions (see Figures 6.7 and 6.8).

The expected background and signal M_T distributions are shown in Fig-

W' Mass (GeV/c^2)	$\mathcal{B}(W' \to e\nu)$	$\sigma \cdot \mathcal{B}(W' \to e\nu)$ (pb)	Expected Events
200	0.108	1.40×10^2	11800
250	0.100	5.87×10^1	5290
300	0.0950	2.78×10^1	2580
350	0.0918	1.42×10^1	1360
400	0.0897	7.57	739
450	0.0883	4.17	409
500	0.0873	2.35	231
550	0.0866	1.33	132
600	0.0861	7.64×10^{-1}	75.5
650	0.0857	4.38×10^{-1}	42.9
700	0.0853	2.50×10^{-1}	24.6
750	0.0851	1.42×10^{-1}	14.0
800	0.0849	8.04×10^{-2}	7.74
850	0.0847	4.48×10^{-2}	4.27
900	0.0845	2.46×10^{-2}	2.31
950	0.0844	1.33×10^{-2}	1.22

Table 6.1: The branching fraction and cross section times branching fraction of $W' \to e\nu$ process at $\sqrt{s} = 1.96$ TeV. The NNLO cross sections are calculated with a code provided by van Neerven (R. Hamberg *et al.*) [30] and using MRST1 PDF set [31]. The expected number of observed events are calculated in 205 pb^{-1}.

ure 6.9.
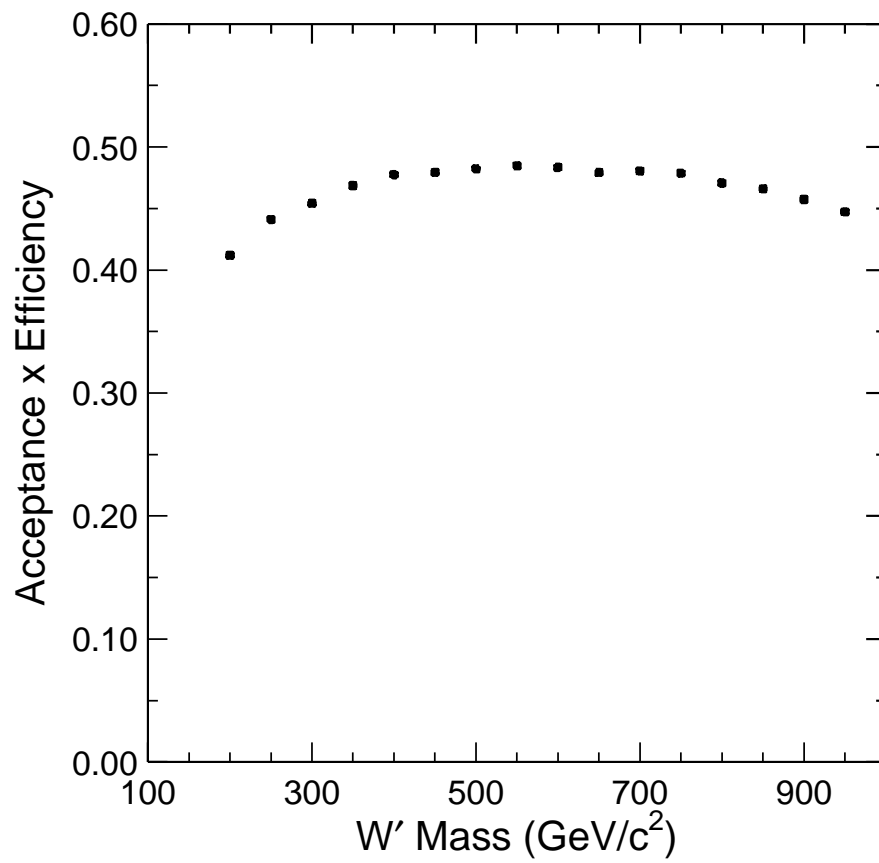
Figure 6.6: Acceptance times event selection efficiency as a function of W' boson mass was calculated using MC. The uncertainties are statistical only.
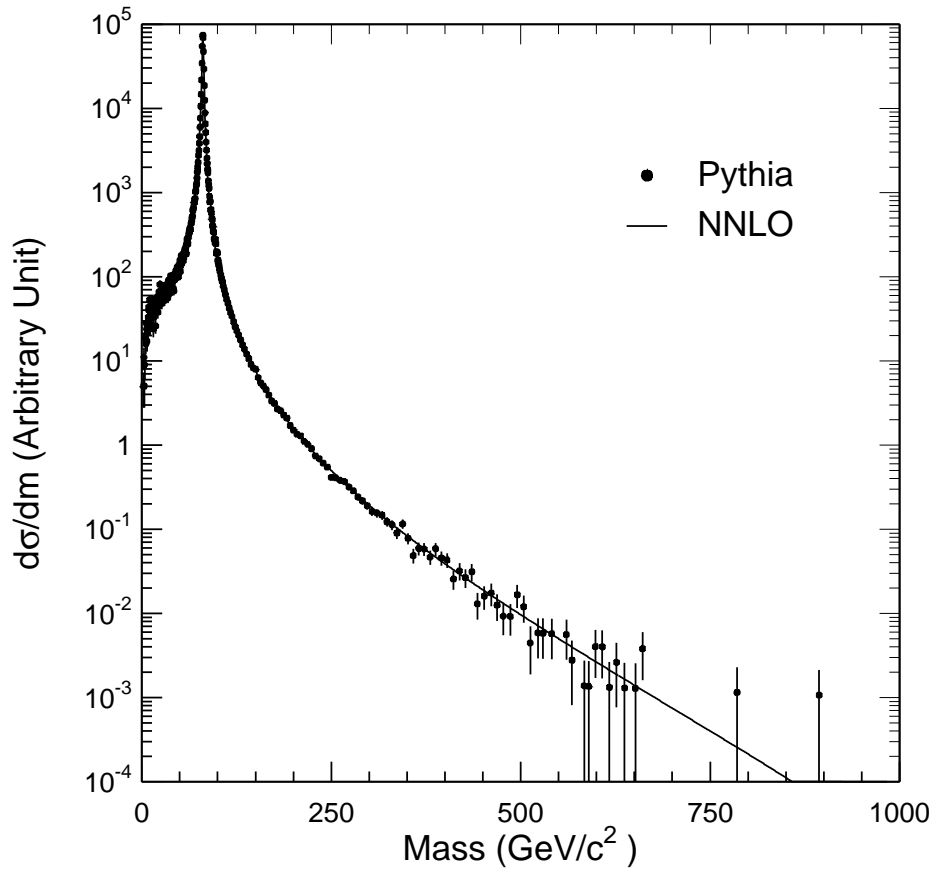
Figure 6.7: $d\sigma/dm$ distribution of W production from PYTHIA (dots) compared to NNLO calculation (line) from Ref. [32]. The uncertainties are statistical only.
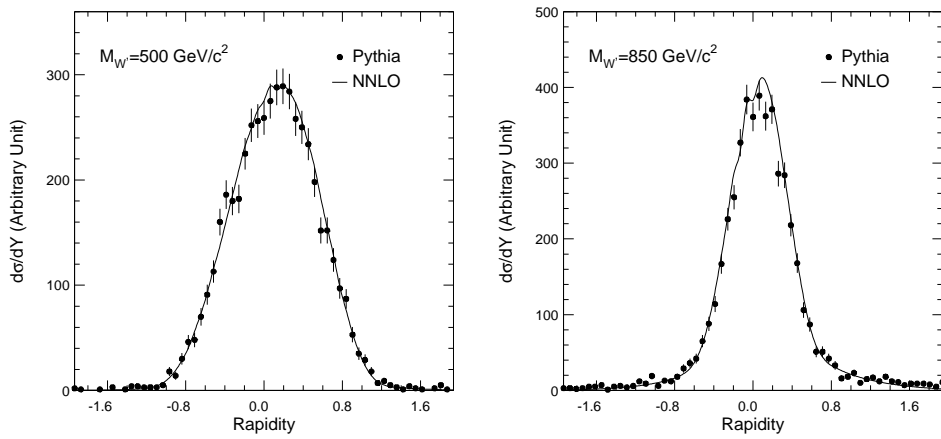
Figure 6.8: Rapidity distributions of 500 GeV/c^2 (left) and 850 GeV/c^2 (right) W' boson from PYTHIA (dots) and NNLO calculations (line) from Ref. [32]. The uncertainties are statistical only.
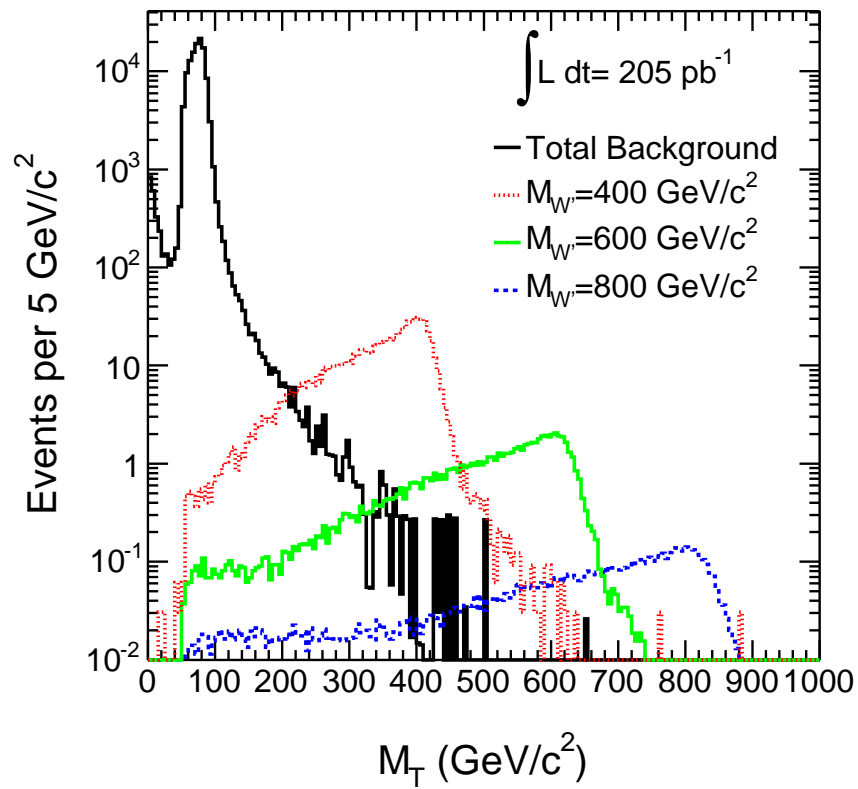
Figure 6.9: The expected M_T distributions in 205 pb^{-1} of data for the background and the signal of $W' \to e\nu$ with $M_{W'} = 400$ GeV/c^2, 600 GeV/c^2, and 800 GeV/c^2.

CHAPTER VII

Background Estimations

As backgrounds to $W' \to e\nu$ process, standard model backgrounds with a real electron and missing energy in final states are considered. There are sources with $W \to e\nu$, $W \to \tau\nu$, $Z/\gamma \to ee$, $Z/\gamma \to \tau\tau$, $t\bar{t}$, and Diboson (WW, WZ). The process of $Z/\gamma \to ee$ can also produce missing energy when one of the electrons from Z/γ events is lost by falling through cracks in the detector. The multijet background comes from events with a misidentified jet as an electron and mismeasured jet energy in the calorimeter, thereby producing a sizable $\not{E}_T$. The detailed description about how to predict each backgrounds are following.

7.1 Standard Model Backgrounds

The expected number of standard model background events in the data is calculated using MC sample by

$$(7.1) \qquad\qquad N_{expected} = \epsilon \cdot A \cdot \sigma \cdot B \cdot \int L dt$$

The ϵ is the combined efficiency of the cut on the electron identification, trigger, and primary vertex of the event. A is the acceptance including kinematic cuts on the leptons and the geometric acceptance of the detector. The total $\epsilon \cdot A$ numbers are calculated with $\epsilon \cdot A = N_{passed}/N_{generated}$ assuming trigger efficiencies to be 1 [1], where N_{passed} is the number of events passed through event selection cuts (described in Chapter IV) from the number of their generated events. The $\sigma \cdot B$ is cross section and branching fraction, and the $\int L dt$ is integrated luminosity recorded by the experiment which corresponds to 205 pb^{-1}. For the cross sections, except for the top and diboson backgrounds which were calculated with NLO, NNLO theoretical cross sections are used.

Table 7.1 shows the predicted number of events for each case of the background in 205 pb^{-1}. The largest background comes from the W decaying to an electron and neutrino pair with B($W \to e\nu$) of 11%. The background of $W \to \tau\nu$ is expected less than $W \to e\nu$ since the background of $W \to \tau\nu$ will have less electrons in final states with B($\tau \to e\nu\nu$) of 17%. The relative expected rate of $Z/\gamma \to ee$ with respect to $W \to e\nu$ events is 9.35×10^{-2}.

---

[1] Any discrepancy in the trigger or event selection efficiencies between data and MC generated events is absorbed by a common normalization factor for the MC generated backgrounds and signal in the fit of M_T distributions. Therefore, this assumption does not affect the results. See Chapter VIII

MC	$\epsilon \cdot A$	$\sigma \cdot B$(pb)	$N_{expected}$
$W \to e\nu$	2.03×10^{-1}	2687 ± 54 (NNLO) [33]	111311
$W \to \tau\nu$	4.38×10^{-3}	2687 ± 54 (NNLO) [33]	2408
$Z/\gamma \to ee$	1.81×10^{-2}	251.3 ± 5 (NNLO) [33]	929
$Z/\gamma \to \tau\tau$	2.72×10^{-3}	251.3 ± 5 (NNLO) [33]	140
WW	9.00×10^{-2}	13.25 ± 0.25 (NLO) [34]	244
WZ	3.56×10^{-2}	3.96 ± 0.06 (NLO) [34]	28.9
$t\bar{t}$	5.11×10^{-2}	6.7 ± 0.5 (NLO) [35]	70.0
Multijet (from DATA)			2808

Table 7.1: The expected background estimations in the $W/W' \to e\nu$ candidate sample in 205 pb^{-1}. We used NNLO cross sections, except for top and diboson backgrounds which were calculated with NLO. The total acceptance numbers are calculated assuming trigger efficiencies to be 1.

The total number of events from the diboson and $t\bar{t}$ backgrounds are not large compared to other backgrounds. However, the high kinematic distributions in the transverse mass are predicted so that those backgrounds will compete in $W' \to e\nu$ signal region.

The M_T distributions of the backgrounds normalized to their expected are shown in Figures 7.1, 7.2, and 7.3.

7.2   Multijet Background

Since dijet events dominate multijet background, in the case of a jet being misidentified as an electron, it will be seen as recoiling against the other jets in the events. Therefore, we expect to see back-to-back behaviour in the azimuthal opening angle between the primary electron candidate and vector summed E_T of all other jets, whereas $W/W' \to e\nu$ process does not have a strong correlation in the opening angle. In order to get the expected number
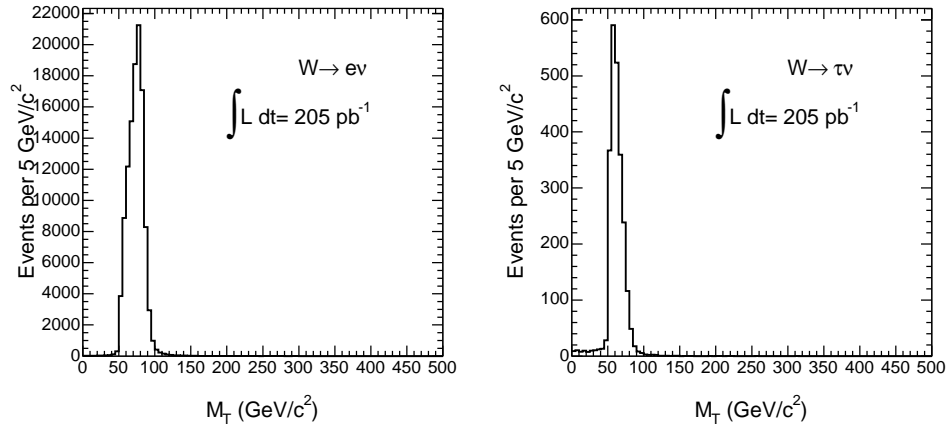
Figure 7.1: The expected $W \rightarrow e\nu$ (left) and $W \rightarrow \tau\nu$ (right) distributions. The distributions are normalized to their expected numbers of events.
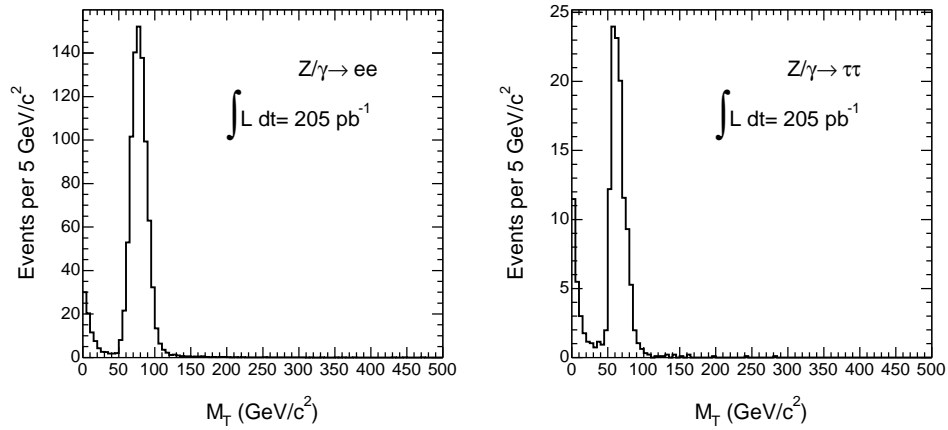
Figure 7.2: The expected $Z \rightarrow ee$ (left) and $Z \rightarrow \tau\tau$ (right) distributions. The distributions are normalized to their expected numbers of events.

67
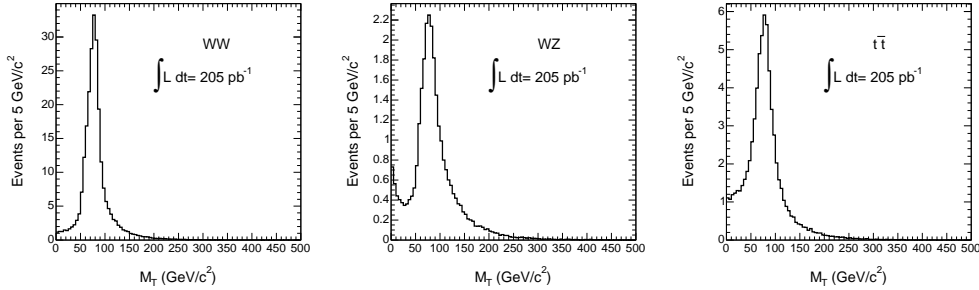
Figure 7.3: The expected WW (left), WZ (middle), and $t\bar{t}$ (right) distributions. The distributions are normalized to their expected numbers of events.

of multijet background events, we apply the method used in $W' \rightarrow \mu\nu$ analysis in Run I [36]. Two samples are created by removing the isolation requirement for $W/W' \rightarrow e\nu$ event candidate sample ($Iso < 0.2$) and using different isolation requirements on the primary electron candidate.

- $Iso < 0.025$ ("Tight" electron enriched sample)

- $Iso > 0.3$ ("Non-isolated" multijet enriched sample)

We calculate the azimuthal opening angle between the primary electron candidate and vector sum of the E_T in each tower but excluding that of the primary electron candidate, $\vec{E}_T^{\not{e}}$:

$$(7.2) \qquad \vec{E}_T^{\not{e}} \equiv \left(\sum_{i=tower} \vec{E}_T^i \right) - \vec{E}_T^e.$$

To estimate the number of multijet background events in $W/W' \rightarrow e\nu$ candidate event sample, we fit the opening angle distributions of $W/W' \rightarrow e\nu$ event sample with that of the electron enriched sample and the multijet

68

enriched sample as shown in Figure 7.4. We use $\vec{E}_T^{\ell}$ variable instead of the vector sum of the E_T of the jets due to the fact that there are events with non clustered jets.

We used a likelihood fitting method to fit the opening angle distribution. The fit was performed only in the range between $\pi/2$ and π, where the shapes fit well. The discrepancy in the low angle region is due to the fact that the electrons that are close to jets with a tight isolation requirement are more likely to fail the requirement than the electrons with a looser cut. We expect that the multijet enriched sample has non negligible contribution from non isolated electrons, mostly coming from $W \rightarrow e\nu$ events. We subtract the expected $W \rightarrow e\nu$ contribution in the opening angle distribution from the multijet enriched sample. The expected contribution of the $W \rightarrow e\nu$ events is calculated using the $W \rightarrow e\nu$ MC sample used for $W \rightarrow e\nu$ background estimation but with the non isolation requirement ($Iso > 0.3$) instead. About $1/4$ of the events in the multijet enriched sample are predicted to be from $W \rightarrow e\nu$ events. From the fit, the number of multijet background events in the $W/W' \rightarrow e\nu$ event candidate sample is determined to be 2808 ± 150 events, where uncertainty is the statistical uncertainty from the fit only and does not include uncertainty coming from the uncertainty in $W \rightarrow e\nu$ contribution.

	Isolation cut	N. of multijet events
"Tight" Electron enriched	Iso < 0.025	
"Non-isolated" multijet enriched	Iso > 0.3	2808 ± 150
"Tight" Electron enriched	Iso < 0.025	
"Semi-non isolated" multijet enriched	0.2 < Iso < 0.25	2691 ± 145
"Loose" electron enriched	Iso < 0.05	
"Non-isolated" multijet enriched	Iso > 0.3	2607 ± 151
"Loose" electron enriched	Iso < 0.05	
"Semi-non isolated" multijet enriched	0.2 < Iso < 0.25	2508 ± 147

Table 7.2: The numbers of multijet background events in four different sample combinations are obtained from the fit in the opening angle between an "electron candidate" and $\vec{E}_T^{\not{}}$.

We build additional samples for the enriched electrons and the enriched multijet to see how stable the number of multijet background events estimate is depending on the isolation cut requirement:

- $Iso < 0.05$ ("Loose" electron enriched sample)

- $0.2 < Iso < 0.25$ ("Semi non-isolated" multijet enriched sample)

The results are shown in Table 7.2. The estimates agree with each other within 3σ.

7.3 Cross Check on the Number of Multijet Background Events

We have used $\Delta\phi(\vec{E}_T^e, \vec{E}_T^{\not{}})$ to estimate the number of multijet background in the $W/W' \rightarrow e\nu$ sample. Here, we consider the "standard" method in CDF, which uses $\not{E}_T$ vs Iso distribution, to cross check the number of multijet background events calculated previously. The basis for this method is the assumption that the $\not{E}_T$ and Iso are not correlated for the multijet
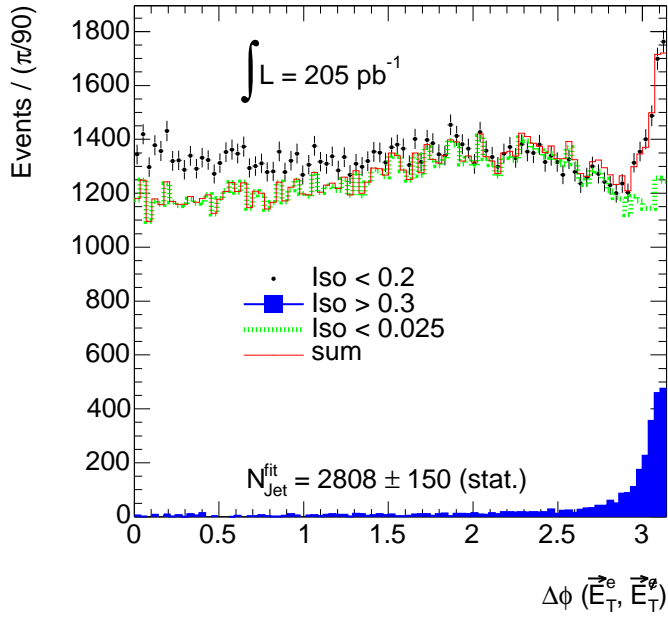
Figure 7.4: The opening angle distributions between the primary electron candidate and $\vec{E}_T^{\ell}$, the vector-summed E_T over energy in towers excluding the primary electron candidate. shown $W/W' \to e\nu$ event sample ($Iso < 0.2$) is fitted with the electron enriched sample ($Iso < 0.025$) and multijet enriched sample ($Iso < 0.3$). The fit range is from $\pi/2$ to π and used likelihood fitting. The $W \to e\nu$ contribution in the multijet enriched sample, which is calculated from MC, is subtracted from the multijet enriched sample.
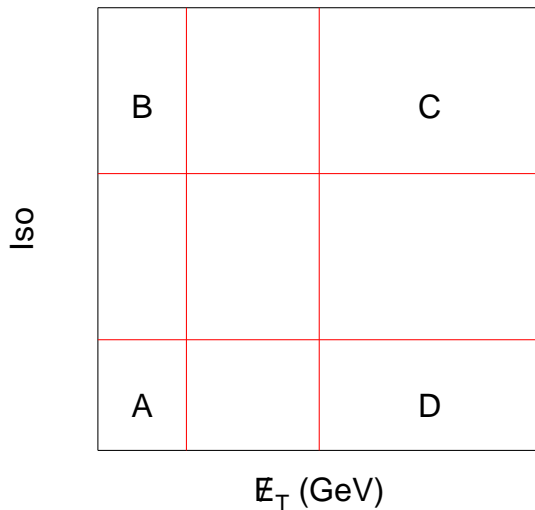
Figure 7.5: Regions in Iso vs $\not{E}_T$ for multijet background calculation. The signal region is represented as "D."

background. The number of multijet background events in the "$W \to e\nu$" signal region (high $\not{E}_T$ and low Iso region), represented as "D" in Figure 7.5, is calculated as

$$(7.3) \qquad\qquad N_D = N_A \times N_C/N_B,$$

where N_i are the number of events in region "i." This method, however, has not been rigorously validated but accepted as correct to a certain degree. In Ref. [37], the ratio, N_C/N_B, is shown to be dependent of Iso, even though the dependence is not shown explicitly.

We used all the event selection cuts listed in Chapter IV except for $\not{E}_T$, Iso, and $E_T/\not{E}_T$ requirements. The last requirement is removed be-

cause it removes events mostly from region "A." Figure 7.6 shows the ratio of number of events in $\not{E}_T > 25$ GeV to that of in $\not{E}_T < 10$ GeV, $n(\not{E}_T > 25 \text{ GeV})/n(\not{E}_T < 10 \text{ GeV})$, at intervals of 0.1 in Iso from 0.2 to 1.0. The contributions from $W \to e\nu$ and $Z \to ee$ are calculated from MC calculations and then subtracted. The dependence on Iso is clearly seen in Figure 7.6. The distribution is fit with an exponetial function

$$(7.4) \qquad \frac{n(\not{E}_T > 25 \text{ GeV})}{n(\not{E}_T < 10 \text{ GeV})} = a \cdot \exp(b \cdot Iso),$$

where the fit parameters a and b are determined to be $(2.55 \pm 0.10) \times 10^{-2}$ and 2.19 ± 0.10, respectively.

Since the Iso distribution of multijet events in the signal region is not known, the area under the fit curve in $0 < Iso < 0.2$ is averaged over the interval to get the average ratio in the signal region. The uncertainty is taken to be a half the difference between the function value at $Iso = 0$ and 0.2. The average ratio in the signal region is $(3.20 \pm 0.70) \times 10^{-2}$. There are 1.85×10^5 events in $\not{E}_T < 10$ GeV and $Iso < 0.2$ region, the expected number of multijet events in the signal region is then $(5.91 \pm 1.29) \times 10^3$ events. This result is consistent within 2σ deviation with the result from $\Delta\phi$ method.

In final, we use the number of multijet events calculated with $\Delta\phi$ method in the case using the sample of $Iso < 0.025$ and $Iso > 0.3$ (see Table 7.2). As for the uncertainty, we take the half the difference between the number

73
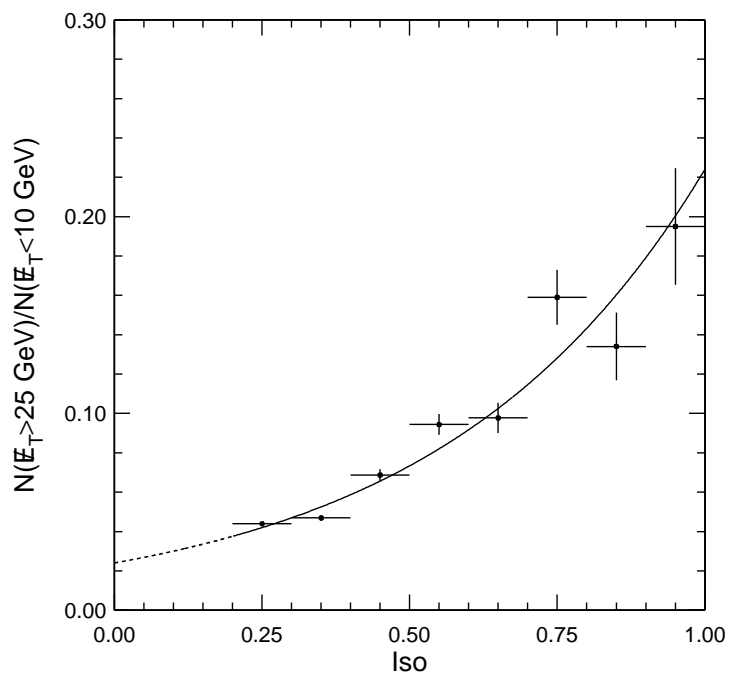
Figure 7.6: The ratio of number of events in $\not{E}_T > 25$ GeV to number of events in $\not{E}_T < 10$ GeV in intervals of 0.1 in Iso. The line shows the fit using an exponetial function. The fit results are given in the text. The uncertainties in the ratio are statistical only. The dashed line shows the extrapolation in the signal region.

74

calculated with $\Delta\phi$ method and the number calculated with the method described in this section for cross-check. The multijet background then becomes 2808 ± 1558 events.

7.4   Multijet Background M_T Shape

The transverse mass distribution of the multijet background can be obtained using non isolated "electron candidate" sample which is the electron sample with anti isolation selection ($Iso > 0.2$), and has a high multijet event content. Since we are using non isolated sample to model the M_T distribution of isolated multijet events, the E_T of the non isolated electron candidate has to be corrected. The isolated misidentified jet deposits most of its energy in the towers contained in the EM cluster. However, the non isolated misidentified jet has multiple particles carrying its energy that is deposited in wider area. Therefore, the EM cluster energy of the non isolated misidentified jet is smaller than that if the isolated misidentified jet for a given initial parton energy. We correct energy of non isolated electron candidates by a factor of $(1 + Iso)$, i.e. $E_T(1 + Iso) \, (= E_T^{fe})$, where $E_T \cdot Iso$ is the energy deposited within the cone of 0.4, excluding the EM cluster energy.[2]

However, this correction introduces a bias in the corrected E_T, E_T^{fe}, at high Iso due to the cut, $E_T > 18$ GeV, made in stripping the data to make

---

[2]This overcorrects E_T somewhat, however.

the data sample used for this analysis. If we have the minimum E_T, E_T^0, and cut on E_T^{fe} at E_T^{fec}, then $E_T^0(1 + Iso)$ is greater than E_T^{fec} when Iso is greater than $E_T^{fec}/E_T^0 - 1$. Therefore, we would have no events between E_T^{fec} and $E_T^0(1 + Iso)$ as illustrated in Figure 7.7. In order to avoid biases introduced in the E_T^{fe} distribution from the data stripping cut, we need to limit Iso to $\leq E_T^{fec}/E_T^0 - 1$. Even though we have $E_T > 18$ GeV from the data stripping cut, we also have $E_T > 18$ GeV in Level 3 and which may cause the threshold effect at E_T near 18 GeV. So we chose $E_T^0 = 20$ GeV, which limits Iso less than 0.25 when $E_T^{fec} = 25$ GeV, which is our E_T cut value for isolated electron candidates.

However, the multijet background M_T distribution suffers from low statistics if we require only the narrow isolation $(0.20 < Iso < 0.25)$ to avoid the bias in the non-isolated electron candidate E_T distribution. The multijet event sample size can be increased if Iso requirement is eased while avoiding introducing the bias in E_T of the non-isolated electron candidates. Figure 7.7 shows a diagram of the $E_T(1 + Iso)$ $(= E_T^{fe})$ vs Iso with constant E_T^{fe} lines at 25, 35, and 50 GeV, and $Iso = 0.2, 0.25, 0.75,$ and 1.5. In order not to introduce biases in E_T^{fe} distribution, E_T^{fe} has to be above $E_T = 20$ GeV, which is a stripping cut applied to the data sample. The shape of E_T^{fe} distribution in the same E_T^{fe} region should be, in principle, the same regardless of isolation, whereas we expect some dependence of $\not{E}_T$

76

shape on Iso.[3] Figure 7.8 shows the M_T distributions of multijet events

samples in different regions of Iso vs E_T^{fe}. The multijet background M_T

distribution is constructed with several M_T distributions in different E_T^{fe}

and Iso regions. The multijet M_T shape distribution is constructed as

$$(7.5) \quad M_T = h00 + \frac{n_{01}}{n_{01} + n_{11}}(h01 + h11) + \frac{n_{02}}{n_{02} + n_{12} + n_{22}}(h02 + h12 + h22),$$

where n_x is the number of events in the histogram hx and the resulting

composite M_T distribution is shown in Figure 7.9. A KS test between the

composite distribution and the original distribution $(0.20 < Iso < 0.25)$ in

solid line in Figure 7.9 gives a probability of $\sim 6\%$.

The resulting distribution with $W \to e\nu$ contribution subtracted is shown

in Figure 7.10.

---

[3]The ratio $\frac{n(35 < \not{E}_T < 50\ GeV)}{n(25 < \not{E}_T < 35\ GeV)}$ is consistent to be constant in $Iso > 0.2$ but $\frac{n(\not{E}_T > 50\ GeV)}{n(25 < \not{E}_T < 35\ GeV)}$ shows dependence at $Iso > \sim 0.7$
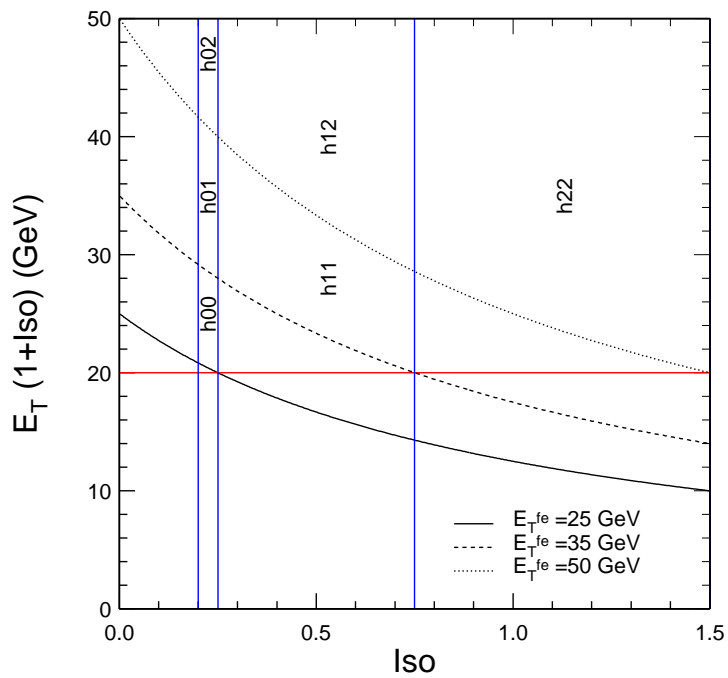
Figure 7.7: The stripping cut, $E_T > 20$ GeV. $h$xx reprensents the M_T distribution of the events surrounded by the lines as described in the text.
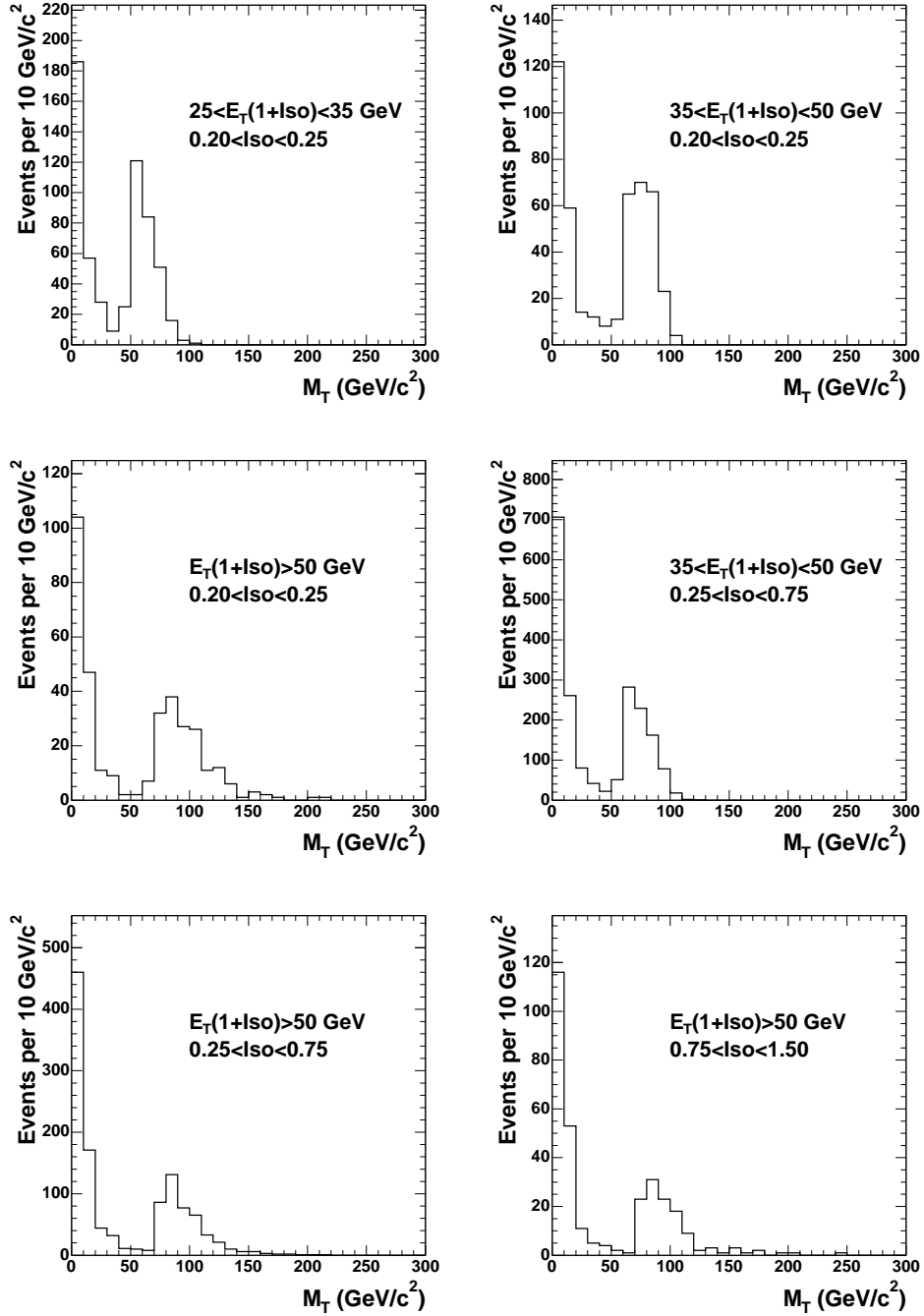
Figure 7.8: The M_T distributions in different regions of $\not{E}_T$ vs Iso shown in Figure 7.7.
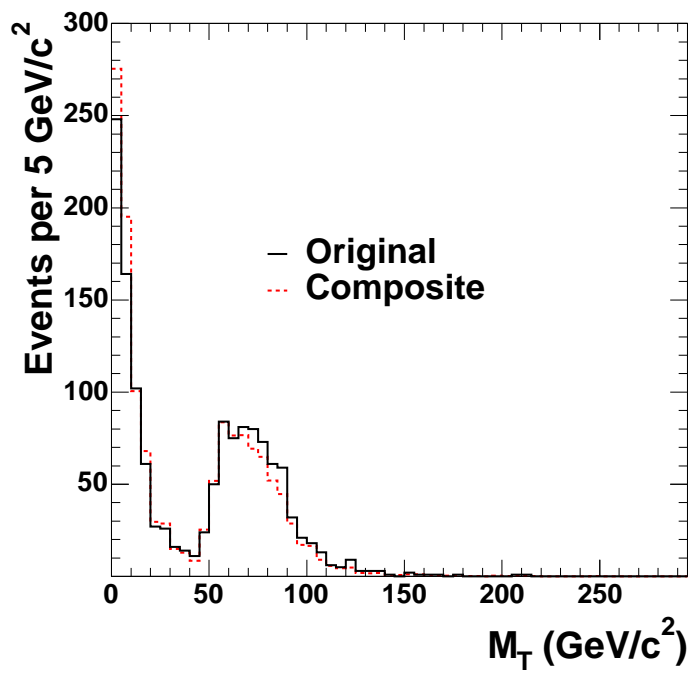
Figure 7.9: Composite multijet background M_T distribution (dashed) and the original distribution (solid) from the region of $0.20 < Iso < 0.25$. The $W \to e\nu$ contribution is not subtracted. Distributions are not normalized to the expected number of multijet events.
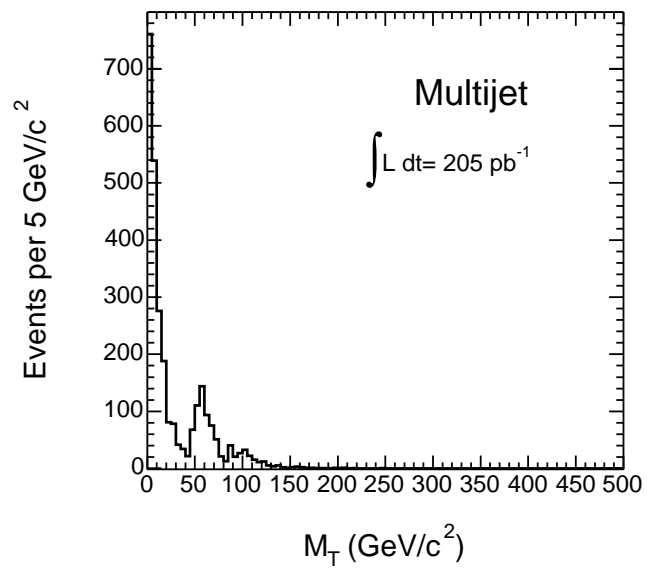
Figure 7.10: The transverse mass distribution of multijet background scaled up to the expected number of events.

CHAPTER VIII

Likelihood Fit of Transverse Mass Distribution

In order to determine the $W' \to e\nu$ signal contribution in $W/W' \to e\nu$ candidate event sample, a binned likelihood fitting method is used. The number of events in the jth bin is

$$(8.1) \qquad \mu^j = \alpha_0 [\sum_{i \neq jet} \mu_i^j + \beta \mu_{sig}^j] + \alpha_{jet} \mu_{jet}^j,$$

where α_0, α_{jet}, and β are the parameters to be determined by the fit, $\mu_i^j (\mu_{jet}^j)$ is the expected number of the ith non-multijet (multijet) background and μ_{sig}^j is that of $W' \to e\nu$ signal in the jth bin. The probability of observing n_o^j events in the jth bin when expecting μ^j events can be written as

$$(8.2) \qquad p(\alpha_0, \alpha_{jet}, \beta) = \left(\prod_j \frac{\mu_j^{n_o^j} e^{-\mu_j}}{n_o^j!} \right) \mathcal{G}(\alpha_{jet}, \sigma_{jet}),$$

where $\mathcal{G}(\alpha_{jet}, \sigma_{jet})$ is

$$(8.3) \qquad \mathcal{G}(\alpha_{jet}, \sigma_{jet}) = \frac{1}{\sqrt{2\pi}\sigma_{jet}} \exp \left(-\frac{1}{2} \left(\frac{\alpha_{jet} - 1}{\sigma_{jet}} \right)^2 \right).$$

This Gaussian term constrains the number of multijet background events to the expected number of multijet events estimated from the data as shown in Section 7.2. The width, σ_{jet}, is $1558/2808 = 0.5548$ as determined in Section 7.3.

The probability is maximized by minimizing the negative log of the probability to get the best fit value. The fit results are shown in Table 8.1. Overall, there are small excesses up to in the wide range of W' mass, especially 350-500 GeV/c^2 mass range with $\sim 2\sigma$ excess. This reflects the excess in the 350-500 GeV/c^2 M_T bin as shown in Figure 8.1 and Table 8.2 where we observe 9 events expecting 4 events. Figure 8.1 shows the fit using only the backgrounds. Table 8.2 shows the expected numbers of background events and observed numbers of data in each M_T bin above $M_T = 200$ GeV/c^2.

W' Mass (GeV/c^2)	α_0	α_{jet}	β ($\times 10^{-2}$)
200	1.019 ± 0.003	1.137 ± 0.026	$0.180^{+0.158}_{-0.144}$
250	1.019 ± 0.003	1.138 ± 0.026	$0.163^{+0.244}_{-0.163}$
300	1.019 ± 0.003	1.139 ± 0.026	$0.143^{+0.322}_{-0.143}$
350	1.019 ± 0.003	$1.138^{+0.027}_{-0.025}$	$0.794^{+0.554}_{-0.473}$
400	1.019 ± 0.003	1.139 ± 0.026	$1.21^{+0.77}_{-0.63}$
450	1.019 ± 0.003	1.139 ± 0.026	$1.90^{+1.21}_{-0.97}$
500	1.019 ± 0.003	1.139 ± 0.026	$2.81^{+1.94}_{-1.49}$
550	1.019 ± 0.003	1.139 ± 0.026	$2.98^{+2.94}_{-2.09}$
600	1.019 ± 0.003	1.139 ± 0.026	$3.36^{+2.60}_{-2.58}$
650	1.019 ± 0.003	1.139 ± 0.026	$4.04^{+6.43}_{-3.58}$
700	1.019 ± 0.003	$1.139^{+0.026}_{-0.025}$	$5.01^{+9.89}_{-5.01}$
750	1.019 ± 0.003	$1.138^{+0.027}_{-0.025}$	$6.0^{+16.2}_{-6.0}$
800	1.019 ± 0.003	1.138 ± 0.026	$7.5^{+27.9}_{-7.5}$
850	1.019 ± 0.003	1.138 ± 0.026	$8.1^{+51.2}_{-8.1}$
900	1.019 ± 0.003	1.138 ± 0.026	6^{+100}_{-6}
950	1.019 ± 0.003	1.139 ± 0.026	0^{+215}_{-0}

Table 8.1: The fit results for the parameters on each W' boson mass point. The fit parameters α_0, α_{jet}, and β are defined in Eq. 8.1. The uncertainties are statistical only.
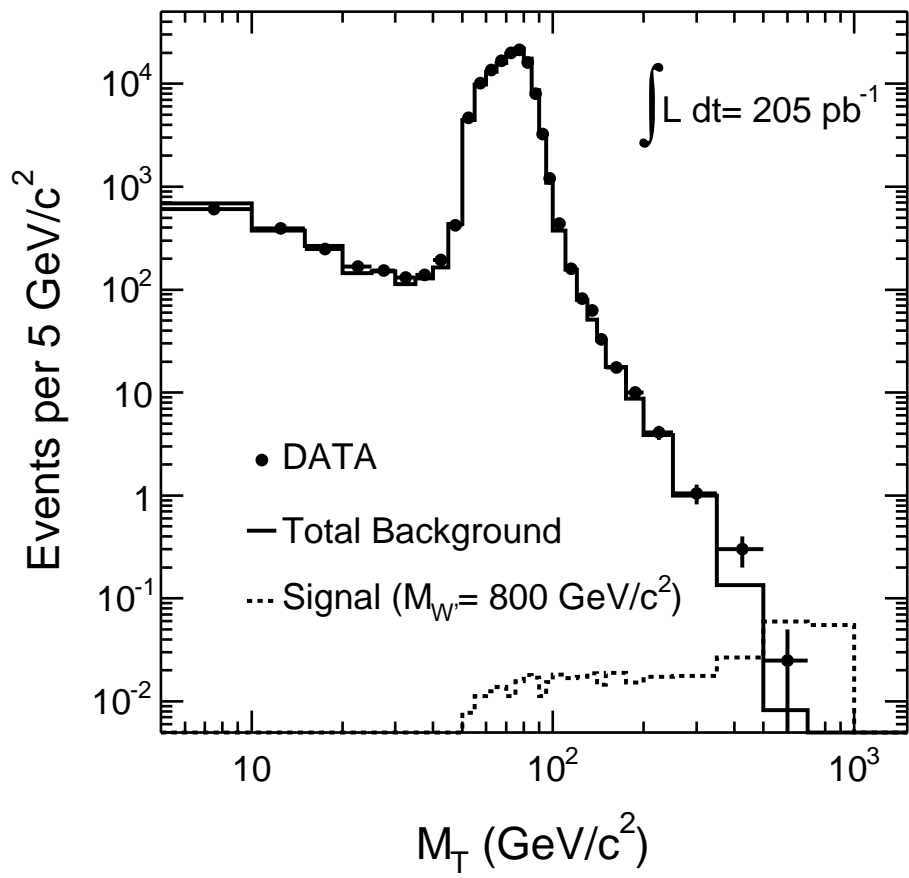
Figure 8.1: The transverse mass distributions of $W/W' \to e\nu$ candidate events in 205 pb^{-1} of data and the standard model backgrounds.

	Events in Each M_T Bin (GeV/c^2)				
	200 - 250	250 - 350	350 - 500	500 - 700	700 - 1000
$W \to e\nu$	30.8 ± 5.7	17.0 ± 4.0	3.52 ± 1.70	0.27 ± 0.45	0.00 ± 0.00
Multijet	2.7 ± 6.1	0.0 ± 3.3	0.00 ± 0.29	0.00 ± 0.01	0.00 ± 0.00
Other Backgrounds	5.2 ± 1.0	3.0 ± 0.9	0.51 ± 0.22	0.06 ± 0.08	0.00 ± 0.03
Total Background	38.7 ± 8.9	20.0 ± 5.9	4.03 ± 1.97	0.33 ± 0.53	0.00 ± 0.03
Data	41	21	9	1	0

Table 8.2: The search results of the binned likelihood fitting method. Shown are expected numbers of standard model background events in each M_T bin above 200 GeV/c^2. The uncertainties on total expected number of events accounts for the correlations in among individual background uncertainties.

86

CHAPTER IX

Systematic Uncertainties

We use a method of constructing a probability distribution $p(\beta)$, which we obtain by maximizing $p(\alpha_0, \alpha_{jet}, \beta)$ shown in Eq. 8.2 for each successive value of β and then multiplying the results with a flat prior. We repeat it for each mass value of the W' boson. We then use a Gaussian convolution method to incorporate the effects of the systematic uncertainties on the probability density [38], where

(9.1)

$$p(\beta) = \int_0^\infty d\beta' p(\beta') \frac{1}{\sqrt{2\pi}\sigma(\beta)} \exp\left(-\frac{(\beta'-\beta)^2}{2(\sigma(\beta))^2}\right) \left(1 + \frac{(\beta'-\beta)}{\sigma(\beta)} \frac{\partial\sigma(\beta)}{\partial\beta}\right).$$

Here $\sigma(\beta)$ is the smearing factor that is constructed with effects of the systematic uncertainties on the probabilities. The extra Jacobian term in the equation is a product of changing the posterior integral over the nuisance parameter to over β. The smearing is done only in the physical region, that is $\beta \geq 0$.

The systematic uncertainty from a given nuisance parameter is calculated with the size of shift in the cumulative probability of $p(\beta)$ for the nuisance parameter shift. The cumulative probability $P(\beta, \nu)$ is defined as $P(\beta, \nu) \equiv \int_{-\infty}^{\beta} p(\zeta, \nu) d\zeta$, where ν is a nuisance parameter. The probability $p(\beta)$ in the integrand in Eq. 9.1 is $p(\beta, \nu_0)$, where ν_0 is the nuisance parameter at its mean (the "default" case). The nuisance parameter shifted probability $p(\beta, \nu)$ is obtained the same way as the default case using nuisance parameter shifted M_T templates to fit the data. The shift, $\delta(\beta)$, is calculated from[1]

(9.2)
$$P(\beta, \nu) = P(\beta + \delta(\beta), \nu_0).$$

Here the integration to obtain the cumulative probability of $p(\beta, \nu)$ is performed only in the physical region [38].

Figure 9.1 shows the probability distributions and their cumulative probability distributions for $400\,\mathrm{GeV}/c^2$ W' boson for the default and the electron energy scale shifted cases. Figure 9.2 shows $\delta(\beta)$ for this particular case.

The shift function $\delta(\beta)$ is obtained for each nuisance parameter as described earlier and is used to perform the Gaussian convolution shown in Eq. 9.1. The smearing factor, $\sigma(\beta)$, in Eq. 9.1 is determined from $\delta(\beta)$ for each systematic uncertainty as described below. The smearing is performed for each nuisance parameter successively. The results are shown in

---

[1]The cumulative probability for $P(\beta, \nu)$ is simply a cumulative probability calculated with the probability density constructed with nuisance parameter shifted M_T distributions in the fit.
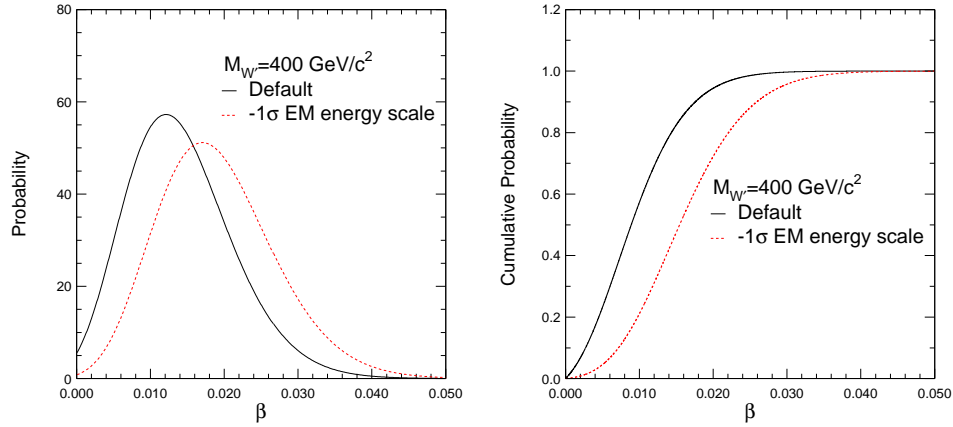
Figure 9.1: The probability distributions for the default case and shifted nuisance parameter, -1σ shift in electron energy scale in this case. The right plot shows the cumulative probability as a function of β, where the integration is done only in the physical region.
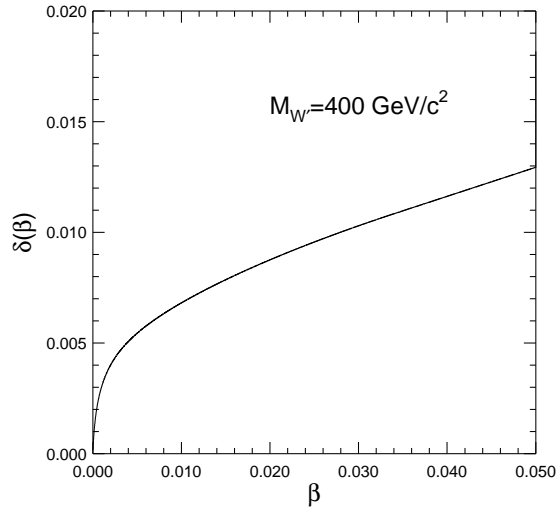

Figure 9.2: The shift $\delta(\beta)$ in the cumulative probability due to a -1σ electron energy scale shift for $M_{W'} = 400$ GeV/c^2 case shown in Figure 9.1.

Figure 9.3. The sources of systematic uncertainties are described below.

9.1 Parton Density Function

The uncertainty stemming from Parton Density Function (PDF) affects the cross sections and the kinematics. However, the limits on the signal cross section are not affected by the uncertainty in the signal cross section. Therefore, we consider uncertainties in the M_T distributions and acceptance of the signal resulting from the uncertainties in PDFs. For backgrounds, the effects of the cross section uncertainty are included. The effects of using various PDFs are calculated by the method advocated by S. Miller and supported by "Joint Physics PDF Accord," in which the events are weighted according to the parton density function recalculated from the parton level kinematics information [39].

The M_T distributions for both signal and backgrounds are made for each PDF set. The signal acceptance is calculated for each PDF set with respect to CTEQ6M set. The signal M_T distributions are normalized with respect to the number of events in the M_T distribution with CTEQ6M then mulitplied by the relative acceptance with respect to the acceptance for the CTEQ6M case. This accounts for the change of the M_T shape and acceptance but removes the effects of the cross section change of the signal. We used these M_T distributions in the fit of the data to extract the uncertainties.

We compared CTEQ6M with 20 eigenvectors shifted up and down and

its default. The smearing factor $\sigma(\beta)$ is calculated as $(|\delta^+(\beta)| + |\delta^-(\beta)|)/2$, where $\delta^\pm(\beta)$ is the size of shift in the cumulative probability of the up/down shift from default.[2] Since these eigenvectors are orthogonal, each eigenvector case is treated as independent.

Also, one of the suggestions at the accord was to compare MRST and CTEQ6M to represent the systematic uncertainty in the momentum transfer scale.[3] As suggested at the accord we used MRST72 compared against CTEQ6M without eigenvector shift. The shift is taken as the additional smearing factor to the above-mentioned PDF uncertainties.

9.2 Electron Energy Scale and Resolution

As mentioned in Section 6.1, the uncertainty in the electron energy scale is taken to be 3%. The electron energy is varied $\pm3\%$. The smearing factor is calculated to be $(|\delta^+(\beta)| + |\delta^-(\beta)|)/2$, where $\delta^\pm(\beta)$ is the shift in the cumulative probability by $\pm1\sigma$ change in the electron energy scale.

As for the uncertainty due to electron energy resolution, we again take the half of $\delta(\beta)$ between the smeared and non-smeared.

---

[2]Taking the average of the absolute values of δs normally does not change the sign of $\frac{1}{\sigma(\beta)}\frac{\partial \sigma(\beta)}{\partial \beta}$ in the Jacobian term, because $\delta(\beta)$ usually is monotonous as shown in Figure 9.2.

[3]This quite possibly double-counts some aspects of the CTEQ6M with 20 eigenvectors and choosing one PDF to compare against is quite arbitrary in itself. And this introduces an arbitrary factor in choosing a PDF to compare with.

9.3 Initial State Radiation

The Initial State Radiation (ISR) results in the distortion of the mass lineshape. We turned ISR off in PYTHIA for signal and compared them against the default case (ISR on). We found that the effect is negligible for low M_T region where background is expected to dominate. Half of shift in the cumulative probability is taken as the uncertainty.

9.4 Jet Energy Scale

We used the function `totalJetSystematics` [40] to get the total $\pm 1\sigma$ shift in the jet energy scale systematics, which calculate the effect of individual jet uncertainties. The jet energy is shifted up and down by this amount and $\not{E}_T$ is recalculated. The smearing factor is taken to be $(|\delta^+(\beta)| + |\delta^-(\beta)|)/2$, where $\delta^\pm(\beta)$ is the shift in the cumulative probability by $\pm 1\sigma$ change in the jet energy scale.

9.5 Relative Fractions of Backgrounds

The relative fraction of each background, except for multijet background, is varied by $\pm 1\sigma$ of its theoretical cross section and then fit the data M_T distribution to obtain the shift the cumulative probability distribution. The smearing factor is taken to be $(|\delta^+(\beta)| + |\delta^-(\beta)|)/2$, where $\delta^\pm(\beta)$ is the shift in cumulative probability by $\pm 1\sigma$ change for each background fraction.

9.6 Multijet Background

Since the multijet background contribution is Gaussian constrained to its expected number of events and uncertainty, we only consider the change in the shape of the multijet M_T distribution. We considered the various ways of changing the shape of the M_T distribution of the multijet background, such as changing the relative fractions of the M_T distributions in the different kinematic regions in the composite M_T distribution (see Section 7.4), changing the non-isolated $W \rightarrow e\nu$ fraction in the multijet sample, and using various functions to fit the high M_T region of the multijet M_T distribution. We found that with $+1\sigma$ change of the non-isolated $W \rightarrow e\nu$ contribution in the multijet sample and using an exponential function for the fit in the high M_T region gives a reasonably large change in the high M_T region (> 250 GeV/c^2), increasing the expected number of events from none to ~ 3 events. We use this modified M_T distribution to estimate the multijet uncertainty.
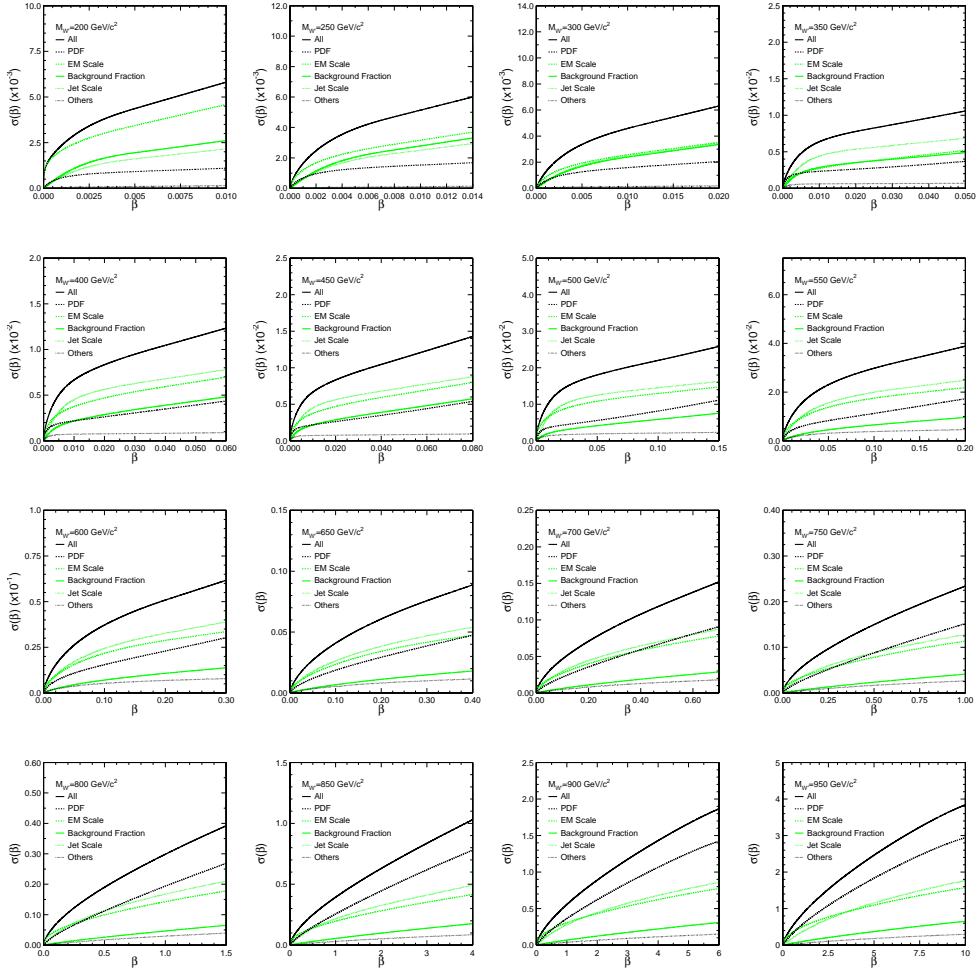
Figure 9.3: The smearing factor $\sigma(\beta)$ in Eq. 9.1 due to systematic uncertainties are shown as a function of β. $\sigma(\beta)$ shown here are summed in several categories, PDF, electron energy scale, background fraction, jet energy scale, and the rest, in quadrature to show their sizes but not used in this summed form for smearing.

94

CHAPTER X

Results

In order to calculate the limit, we start from Eq. 9.1. First, we construct a probability distribution as described in Chapter IX. We then incorporate the systematic uncertainties into the probability densities using a method of Gaussian convolution shown in Eq. 9.1 in Chapter IX. The smearing is done only in the physical region, that is $\beta \geq 0$. The unsmeared and smeared probability densities are shown in Figure 10.1.

The 95% confidence level limit in terms of β is calculated by

$$(10.1) \qquad 0.95 = \frac{\int_0^{\beta_{95}} p(\beta)d\beta}{\int_0^\infty p(\beta)d\beta},$$

where $p(\beta)$ is the smeared probability distribution and β_{95} is the 95% CL limit on $\beta = \frac{\sigma \cdot \mathcal{B}(W' \to e\nu)}{\sigma \cdot \mathcal{B}(W' \to e\nu)_{SM}}$. Here $\sigma \cdot \mathcal{B}(W' \to e\nu)_{SM}$ is the cross section times branching fraction of $W' \to e\nu$ process assuming the standard model strength couplings. The limits are shown in Table 10.1 and Figure 10.2. Also, if we assume that W' boson has the standard model strength couplings,
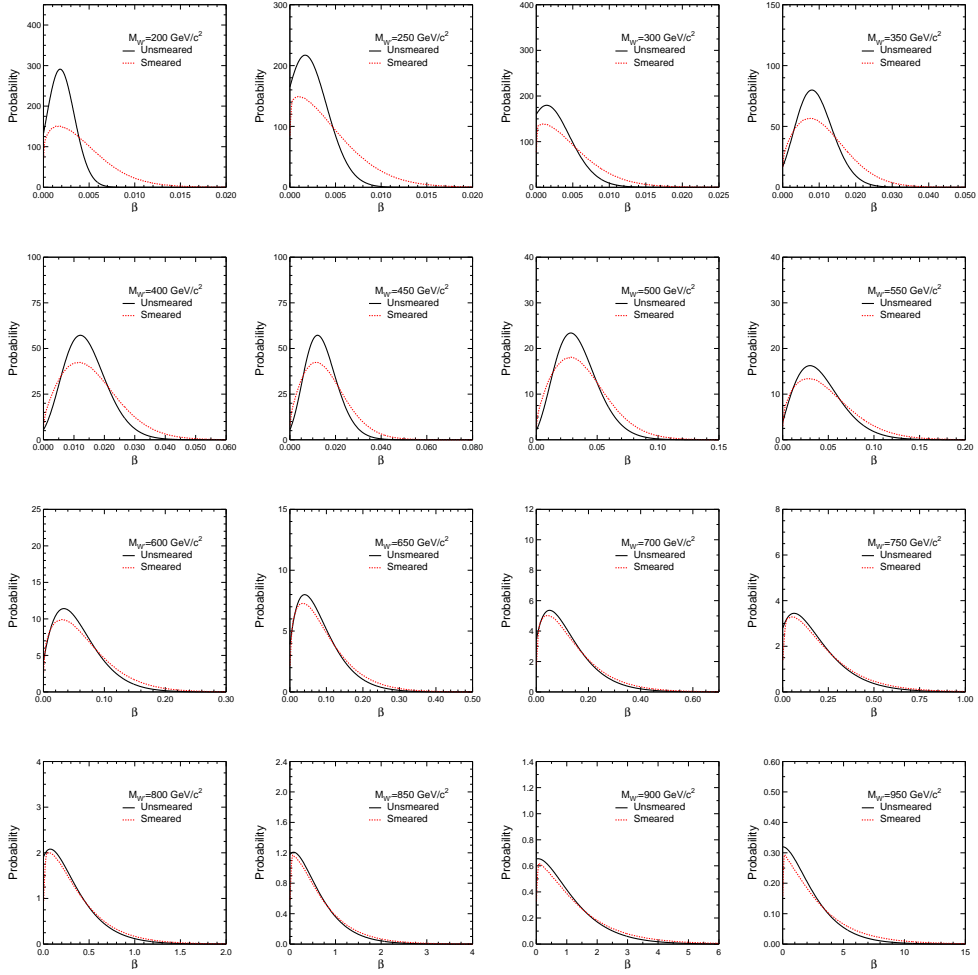
95

Figure 10.1: Probability densities before (solid) and after (dashed) systematic uncertainty smearing.

we can set the lower mass limit at the mass value at $\beta_{95} = 1$, which is where the cross section limit curve and the expected cross section with standard model strength curve cross each other. We incorporated uncertainties on the cross section setmming from PDF uncertainties and the momentum transfer scale. We calculated the uncertainties due to PDFs by calculating the cross section with CTEQ6M and varying 20 eigenvectors shifted up and down. We took the differences of these calculated numbers from the cross section calculated using the default CTEQ6M and symmetrised for each eigenvector and added in quadrature. We calculated the differences in cross section $Q^2 = M_{W'}^2$ using momentum transfer scales of $Q/2$ and $2Q$. The uncertainties from PDFs and momentum transfer scale are added in quadrature. We took the lower cross section of the two and the cross section limit to get the mass limit. The mass limit is found to be $M_{W'} > 788 \text{ GeV}/c^2$ with theoretical uncertainty on cross section and $> 800 \text{ GeV}/c^2$ without the uncertainty. We also set the limits on the ratio of the coupling constants, g_R/g_L, where $g_R/g_L = \sqrt{\beta}$, assuming LR symmetric model. The limits are shown in Figure 10.3.

The expected limits are calculated using pseudo-experiments by generating backgrounds with their expected numbers of events. The expected number of events for each background is fluctuated according to Poisson probability with its mean at the expected number of events when gener-
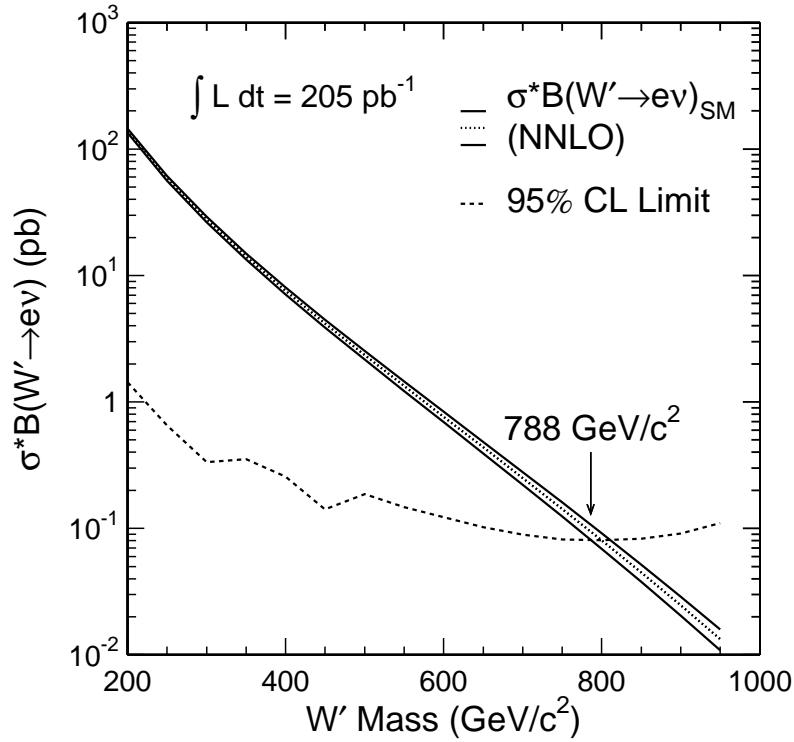
Figure 10.2: The 95% CL limits on cross section times braching fraction. The region above the curve is excluded by 95% CL. Also the cross section times braching fraction assuming the standard model strength couplings is shown. The uncertainty on the theoretical cross section is shown as a band, which is calculated with changes in the CTEQ6M eigenvector shift and the momentum transfer scale change. Assuming the standard model strength couplings, the intercept of the lower cross section curve and the limit on the cross section curve yields $M_{W'} > 788$ GeV/c^2 at 95% CL. Without the theoretical uncertainty on cross section, the mass limit is $M_{W'} > 800$ GeV/c^2.

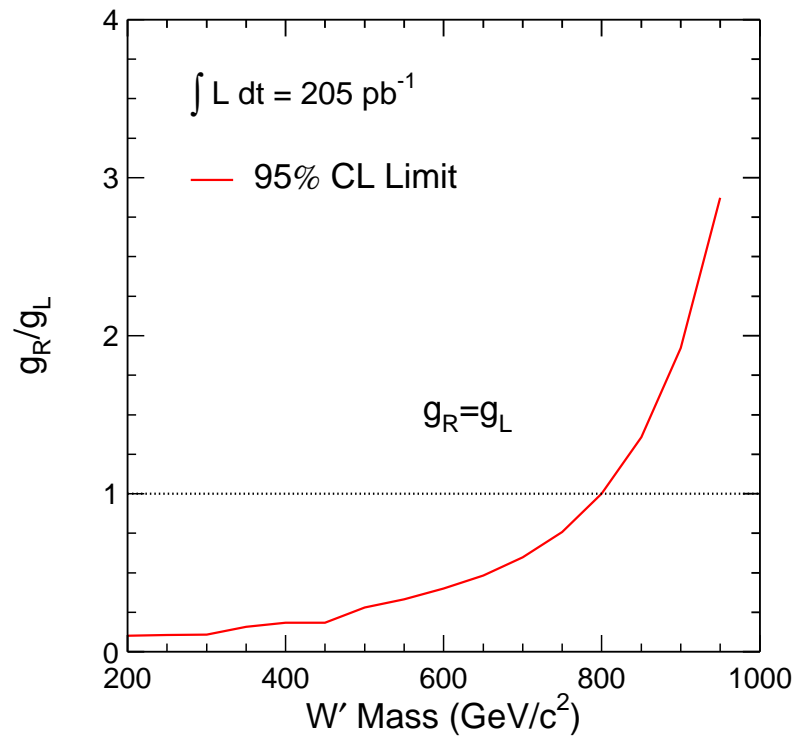Figure 10.3: The 95% CL limits on standard model strength couplings is shown.

W' Mass (GeV/c^2)	β_{95}	$\sigma \cdot \mathcal{B}(W' \to e\nu)_{SM}$	$\sigma \cdot \mathcal{B}(W' \to e\nu)_{95}$
200	1.02×10^{-2}	1.40×10^2	1.43
250	1.11×10^{-2}	5.87×10^1	6.54×10^{-1}
300	1.20×10^{-2}	2.78×10^1	3.34×10^{-1}
350	2.49×10^{-2}	1.42×10^1	3.52×10^{-1}
400	3.40×10^{-2}	7.57	2.57×10^{-1}
450	3.40×10^{-2}	4.17	1.42×10^{-1}
500	7.94×10^{-2}	2.35	1.86×10^{-1}
550	1.11×10^{-1}	1.33	1.48×10^{-1}
600	1.61×10^{-1}	7.64×10^{-1}	1.23×10^{-1}
650	2.34×10^{-1}	4.38×10^{-1}	1.02×10^{-1}
700	3.57×10^{-1}	2.50×10^{-1}	8.92×10^{-2}
750	5.73×10^{-1}	1.42×10^{-1}	8.16×10^{-2}
800	1.00	8.04×10^{-2}	8.04×10^{-2}
850	1.84	4.48×10^{-2}	8.26×10^{-2}
900	3.70	2.46×10^{-2}	9.12×10^{-2}
950	8.26	1.33×10^{-2}	1.10×10^{-1}

Table 10.1: The 95% CL limits on the signal contribution, β_{95}, cross section times branching fraction of $W' \to e\nu$ process assuming the standard model strength couplings, and their 95% CL limits (unit : pb).

ating pseudo-experiments. We performed $\sim 50\,000$ pseudo-experiments for each mass point and calculated the expected limits the same way we did for the data, except incorporating the systematic uncertainties. The results are shown in Figure 10.4. The expected limits are lower than the measured limits by 2σ above $M_{W'} = 350$ GeV/c^2, reflecting the excess in 350-500 GeV/c^2 bin in the M_T distribution shown in Figure 8.1 and Table 8.2.
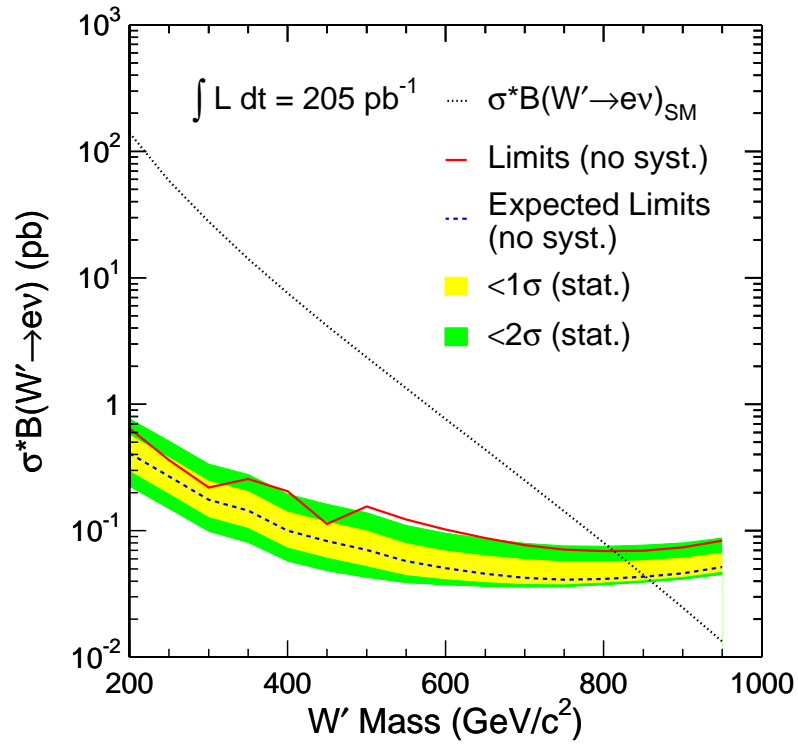
Figure 10.4: The 95% CL limits on $\sigma \cdot \mathcal{B}(W' \to e\nu)$ with statistical uncertainties (solid) and the expected limits (dashed). The uncertainty on the expected limits are shown as bands, for 1σ and 2σ. The $\sigma \cdot \mathcal{B}(W' \to e\nu)$ with standard model coupling strength is shown in dotted curve.

CHAPTER XI

Conclusion

The heavy charged vector boson W' was searched for in an electron and neutrino pair final state using a data sample recorded by the Collider Detector at Fermilab corresponding to an integrated luminosity of (205 ± 12) pb^{-1} of $p\bar{p}$ collisions at $\sqrt{s} = 1.96$ TeV. We do not observe any statistically significant excess over background expectations. We set limits on $\sigma \cdot \mathcal{B}(W' \rightarrow e\nu)$. We set the lower mass limit at $M_{W'} > 788$ GeV/c^2 at 95% CL assuming the standard model strength couplings.

BIBLIOGRAPHY

[1] J.C. Pati and A. Salam, Phys. Rev. D **10**, 275 (1974); R.N. Mohapatra and J.C. Pati, Phys. Rev. D **11**, 566 (1975); *ibid.* Phys. Rev. D **11**, 2558 (1975); G. Senjanovic and R.N. Mohapatra, Phys. Rev. D **12**, 1502 (1975).

[2] R.N. Mohapatra and R.E. Marshak, Phys. Rev. Lett. **44** 1316 (1980).

[3] R.N. Mohapatra and G. Senjanovic, Phys. Rev. Lett. **44** 912 (1980); Phys. Rev. D **23** 165 (1981).

[4] P. Langacker and S. Uma Sankar, Phys. Rev. D **40**, 1569 (1989).

[5] D. E. Groom *et al.* [particle Data Group Collaboration], Eur. Phys. J.C **15**, 1 (2000).

[6] G. Beall, M. Bander, and A. Soni, Phys. Rev. Lett. **48** 848 (1982).

[7] John F. Gunion, Howard E. Haber, Gordon Kane, Sally Dawson "The Higgs Hunter's Guide", Pp. 322-337, (Addison-Wesley Publishing Company, 1990)

[8] PYTHIA 6.2, Physics and Manual, Pp. 91-98, 2001.

[9] F. Halzen and A. D. Martin, *Quarks & Leptons*: An Introductory Course in Modern Particle Physics, Pp. 171, (John Wiley & Sons, NY, 1984).

[10] Vernon D. Barger and Roger J. N. Phillips, *Collider Physics*, Pp. 236-241, (1987).

[11] G. Altarelli, B. Mele, and M. Ruiz-Altaba, Z. Phys. C **45**, 109 (1989).

[12] CDF Collaboration, F. Abe *et al.*, Phys. Rev. Lett. **79**, 2129 (1997).

[13] CDF Collaboration, T. Affolder *et al.*, Phys. Rev. Lett. **87**, 231803 (2001).

[14] M. Czakon, J. Gluza, and M. Zralek, Phys. Lett. B **458**, 355 (1999).

[15] The good run list used is
http://www-cdf.fnal.gov/internal/dqm/goodrun/v4/goodv4.html

[16] J-F Arguin *et al.*, "Jet Corrections for Summer 2003 Analyses (Offline Version 4.10.4)," CDF Note 6565 (2003).

[17] J-F Arguin, A.A. Bhatti, C.A. Currat, R. Erbacher, A. Galtieri, R. Harris, B. Heinemann, H.S. Kim, G. Latino, J. Lys, R. Madrak, M. Martinez, W. Sakumoto, M. Shochet, M. Schmitt "Generic Jet Energy Corrections for Run II data used for the Winter Conferences," CDF Note 6280 (2003).

[18] Koji Ikado, Kaori Maeshima, Tim Nelson, and Muge Karagoz Unel, "Search for New Physics in High Mass Dielectrons," CDF Note 6746 (2003).

[19] Muge Karagoz Unel, Michael Schmitt, Kaori Maeshima, and Koji Ikado, "Searches for New Particles in High Mass Dimuon Channel in CDF Run II Data," CDF Note 6344 (2003).

[20] Young-Kee Kim, Jason Nielsen, Lauren Tompkins & Greg Veramendi. "Trigger Efficiencies for High P_T Electrons", CDF Note 6234 (2003).

[21] Koji Ikado, Ph.D. thesis, Waseda University, 2004, (unpublished).

[22] L. Nodulman, private communication (2005).

[23] T. Sjöstrand *et al.*, Comput. Phys. Commun. **135**, 238 (2001).

[24] H. L. Lai *et al.*, Eur. Phys. J. C **12**, 375 (2000).

[25] M. L. Mangano *et al.*, JHEP **0307**, 001 (2003).

[26] G. Corcella *et al.*, JHEP **0101**, 010 (2001).

[27] Chris Green, Jim Kowalkowsi and Marc Paterno. "*CDF Simulation Framework Developer's Guide*". CDF Note 5369 (2000).

[28] This is called manifest left-right symmetric model. For detailed discussion, see A. Masjero, R. N. Mohapatra, and R. Peccei. Nucl. Phys. **B**192, 66 (1981); J. Basecq, *et al.*, Nucl. Phys. **B**272, 145 (1986).

[29] F. Abe *et al.*, Phys. Rev. D **63**, 011101R (2000).

[30] R. Hamberg, W.L. van Neerven, and T. Matsuura, Nucl. Phys. B **359**, 343 (1991). This code was revised in 2002.

[31] A. D. Martin, R. G. Roberts, W. J. Stirling. and R. S. Thorne, Eur. Phys. C **4**, 463 (1998).

[32] C. Anastasiou, L. J. Dixon, Z. Bern, and D. A. Kosower, Phys. Rev. D **69**, 094008 (2004).

[33] R. Hamberg, W.L. van Neerven, and T.Matsuura, Nucl. Phys. B **39**, 343 (1991); **644**, 403 (E) (2002). R.V. Harlander and W.B. Kilgore, Phys. Rev. Lett. **88**, 201801 (2002); W.K. Sakumoto, "*W/Z Cross Section Prediction Errors for $\sqrt{s} = 1.96$ TeV*," CDF Note 6899 (2004).

[34] J.M. Campbell and R.K. Ellis, Phys. Rev. D **60**, 113006 (1999).

[35] M. Cacciari *et al.,* JHEP **0404**, 068 (2004); N. Kidonakis and R. Vogt, Phys. Rev. D **68**, 114014 (2003).

[36] Hyunsoo Kim, "The $W' \to \mu\nu$ Search in Run 1A and Run 1B," CDF Note 4566 (1998).

[37] D. Amidei *et al.*, "Measurement of $\sigma \cdot B(W \to e\nu)$, $\sigma \cdot B(Z \to ee)$ and $R = \frac{\sigma \cdot B(W \to e\nu)}{\sigma \cdot B(Z \to ee)}$ using CDF Run II Data," CDF Note 6681 (2004).

[38] Luc Demortier, "*Bayesian Treatments of Systematic Uncertainties*," Proceedings of Advanced Statistical Techniques in Particle Physics, Pp145-151, (2002); Luc Demortier, "*A Convolution Method for Folding Systematic Uncertainties into Likelihood Function*," CDF Note 5305 (2005).

[39] `http://cdfrh0.grid.umich.edu/∼miller/pdf/pdf_acceptance.html`

[40] `http://www-cdf.fnal.gov/internal/physics/top/jets/systematics.html`

Acknowledgements

Reminding me of when I had the most hard time at Fermilab, I would like to thank my analysis supervisor Dr. Hyunsoo Kim first and foremost. This analysis could not have been finished without his ceaseless helps. I can not omit his patient answers in so many words even for my stupid questions. I am deeply grateful to him for the invaluable guide and support, always taking my side, no matter what I decided on this analysis throughout my graduation.

I would like to acknowledge my adviser Prof. DongHee Kim for giving me the opportunity to research in CDF experiment at Fermilab, and for providing much encouragement and support during the whole Ph.D. course.

Many thanks to CDF exotic physics group people for the concerned discussions on this analysis. Specially I would like to thank Stephan Lammel, Beate Heinemann, and Song Ming Wang who have been the group conveners. Also thanks are due to Daniela Bortoletto, Wolfgang Wagner, Michael A. Houlden, and Luc Demortier who let me have deeper understanding on the statistical issues.

Abstract

Search for a New Charged Heavy Vector Boson Decaying to an $e\nu$ Pair in

$p\bar{p}$ Collisions at $\sqrt{s} = 1.96$ TeV

by

Jieun Kim

We present results on a seach for a heavy charged vector boson, W', decaying to an electron-neutrino pair in $p\bar{p}$ collisions at $\sqrt{s} = 1.96$ TeV using a data sample corresponding to an integrated luminosity of 205 pb^{-1}. We found no evidence of this decay channel, and set 95% confidence level limits on the production cross section times branching fraction assuming the light neutrino. We also set the limit on the W' boson mass at $M_{W'} > 788$ GeV/c^2, assuming the standard model strength couplings.